Inorganic Chemistry

pubs.acs.org/IC Article

Magnetic Properties and Electronic Structure of the $S = 2$ Complex $[Mn^{III}\{(OPPh_2)_2N\}_3]$ Showing Field-Induced Slow Magnetization Relaxation

Yiannis Sanakis,* J. Krzystek,* Dimitrios Maganas, Alexios Grigoropoulos, Eleftherios Ferentinos, Marios G. Kostakis, Vasiliki Petroulea, Michael Pissas, Komalavalli Thirunavukkuarasu, Wolfgang Wernsdorfer, Frank Neese, and Panayotis Kyritsis*

Cite This: *Inorg. Chem.* 2020, 59, 13281−13294 Read Online

ACCESS | Metrics & More | Article Recommendations | Supporting Information

ABSTRACT: The high-spin $S = 2$ Mn(III) complex $[Mn\{(OPPh_2)_2N\}_3]$ ($\mathbf{1_{Mn}}$) exhibits field-induced slow relaxation of magnetization (*Inorg. Chem.* **2013**, *52*, 12869). Magnetic susceptibility and dual-mode X-band electron paramagnetic resonance (EPR) studies revealed a negative value of the zero-field-splitting (zfs) parameter D. In order to explore the magnetic and electronic properties of $\mathbf{1_{Mn}}$ in detail, a combination of experimental and computational studies is presented herein. Alternating-current magnetometry on magnetically diluted samples ($\mathbf{1_{Mn}}/\mathbf{1_{Ga}}$) of $\mathbf{1_{Mn}}$ in the diamagnetic gallium analogue, $[Ga\{(OPPh_2)_2N\}_3]$, indicates that the slow relaxation behavior of $\mathbf{1_{Mn}}$ is due to the intrinsic properties of the individual molecules of $\mathbf{1_{Mn}}$. Investigation of the single-crystal magnetization of both $\mathbf{1_{Mn}}$ and $\mathbf{1_{Mn}}/\mathbf{1_{Ga}}$ by a micro-SQUID device reveals hysteresis loops below 1 K. Closed hysteresis loops at a zero direct-current magnetic field are observed and attributed to fast quantum tunneling of magnetization. High-frequency and -field EPR (HFEPR) spectroscopic studies reveal that, apart from the second-order zfs terms (D and E), fourth-order terms (B_4^m) are required in order to appropriately describe the magnetic properties of $\mathbf{1_{Mn}}$. These studies provide accurate spin-Hamiltonian (sH) parameters of $\mathbf{1_{Mn}}$, i.e., zfs parameters $|D| = 3.917(5)$ cm^{-1}, $|E| = 0.018(4)$ cm^{-1}, $B^0_4 = B_4{}^2 = 0$, and $B_4{}^4 = (3.6 \pm 1.7) \times 10^{-3}$ cm^{-1} and $\mathbf{g} = [1.994(5), 1.996(4), 1.985(4)]$, and confirm the negative sign of D. Parallel-mode X-band EPR studies on $\mathbf{1_{Mn}}/\mathbf{1_{Ga}}$ and CH_2Cl_2 solutions of $\mathbf{1_{Mn}}$ probe the electronic−nuclear hyperfine interactions in the solid state and solution. The electronic structure of $\mathbf{1_{Mn}}$ is investigated by quantum-chemical calculations by employing recently developed computational protocols that are grounded on ab initio wave function theory. From computational analysis, the contributions of spin−spin and spin−orbit coupling to the magnitude of D are obtained. The calculations provide also computed values of the fourth-order zfs terms B_4^m, as well as those of the $\mathbf{g}$ and hyperfine interaction tensor components. In all cases, a very good agreement between the computed and experimentally determined sH parameters is observed. The magnetization relaxation properties of $\mathbf{1_{Mn}}$ are rationalized on the basis of the composition of the ground-state wave functions in the absence or presence of an external magnetic field.

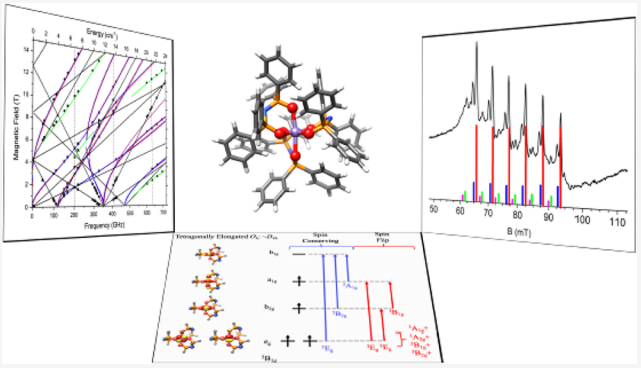

INTRODUCTION

The discovery of multinuclear metal complexes exhibiting slow relaxation of magnetization, referred to as single-molecule magnets (SMMs), has been a hallmark in the field of molecular magnetism.[1] These materials could potentially be used as information storage or molecular spintronic devices for the design of quantum computers,[2−4] and they also exhibit interesting magnetothermal properties.[5] The desired characteristics of multinuclear SMMs are a spin ground state with a large total spin S[6] and a large magnetic anisotropy, expressed via its axial zero-field-splitting (zfs) component (D).[7] These two intrinsic electronic properties dictate the magnitude of the thermal barrier (Δ) for the reversal of magnetization.

The $S = 10$ mixed-valence Mn(III,IV) complex $[Mn_{12}O_{12}(CH_3CO_2)_{16}(H_2O)_4]$ was the first example of a multinuclear complex exhibiting SMM behavior.[8] Following

Received: June 3, 2020
Published: September 8, 2020

https://dx.doi.org/10.1021/acs.inorgchem.0c01636
Inorg. Chem. 2020, 59, 13281−13294

this archetypal molecular magnetic system, a large number of multinuclear complexes with large S spin ground states have been explored.[9] However, such multinuclear systems usually exhibit only small magnetic anisotropies,[10−12] counteracting the favorable effect of a high S value on the magnitude of the effective energy barrier due to which SMMs exhibit slow relaxation of magnetization.[13]

In an alternative approach, research efforts have been directed toward mononuclear complexes of lanthanides and actinides exhibiting large magnetic anisotropy, as well as blocking temperatures (T_B)[14] approaching,[15−17] or even surpassing,[18] that of liquid nitrogen (77 K). There has also been an increased interest in exploring mononuclear transition-metal-based complexes, by both experimental[19−22] and computational methods.[23,24] Collectively, the above complexes are referred to as either mononuclear SMMs or single-ion magnets (SIMs).[22]

Despite the fact that a large number of multinuclear manganese complexes exhibiting SMM behavior contain Mn(III) centers,[9,25] only since 2013 have mononuclear Mn(III) complexes been shown to exhibit (field-induced) slow relaxation of magnetization.[19−22,26−40] Among these compounds, the $[Mn\{(OPPh_2)_2N\}_3]$ complex ($\mathbf{1}_{Mn}$), initially reported by Silvestru and co-workers,[41] has been investigated by some of us by direct- (dc) and alternating-current (ac) magnetometry and dual-mode X-band electron paramagnetic resonance (EPR) spectroscopy.[28] These studies showed that $\mathbf{1}_{Mn}$ exhibits field-induced slow relaxation of its magnetization, which is associated with the presence of zfs in this $S = 2$ system. The combination of dc magnetometry and X-band EPR spectroscopic studies provided initial estimates of the zfs parameters ($D = -3.4$ cm^{-1} and $E/D = 0.11$). Similar studies by X-band EPR have been carried out on other $S = 2$ Mn(III) compounds.[42−48] However, it is not possible to accurately determine, by dc magnetometry and/or X-band EPR alone, the accurate values of all spin-Hamiltonian (sH) parameters, namely, the $\mathbf{g}$ tensor as well as the axial D, rhombic E, and higher-order (for $S \geq 2$)[49] zfs components. In the work presented herein, high-frequency and -field EPR (HFEPR) spectroscopy[50−52] is employed, which has proven to be the appropriate method of choice, allowing for a more accurate determination of the sH parameters, including the higher order zfs terms.[26,27,48,53−73] This is of paramount importance because both the rhombic E and higher order zfs terms provide fast relaxation pathways.[74,75] Moreover, in an effort to probe the operating mechanism of magnetic relaxation, magnetically diluted samples of $\mathbf{1}_{Mn}$ in the diamagnetic analogue $[Ga\{(OPPh_2)_2N\}_3]$ ($\mathbf{1}_{Ga}$)[76] are prepared and investigated by ac magnetometry and X-band EPR. These studies reveal electronic−nuclear hyperfine interactions in the magnetically diluted solid $\mathbf{1}_{Mn}/\mathbf{1}_{Ga}$ systems. Additionally, single-crystal magnetization of both $\mathbf{1}_{Mn}$ and $\mathbf{1}_{Mn}/\mathbf{1}_{Ga}$ is investigated by a micro-SQUID device. Last, the electronic structure of $\mathbf{1}_{Mn}$ is probed by wave-function-based ab initio quantum-chemical calculations, affording sH parameters and probing the involvement of higher-order zfs terms in the magnetization relaxation mechanism of $\mathbf{1}_{Mn}$. When the above experimental and computational findings are combined, the underlying factors imparting field-induced slow relaxation of magnetization in this $S = 2$ octahedral Mn(III) complex are discerned and discussed.

MATERIALS AND METHODS

Chemical Synthesis. Compounds $\mathbf{1}_{Mn}$[28,41] and $\mathbf{1}_{Ga}$[76] were prepared by following the procedures reported in the literature. Magnetically diluted $\mathbf{1}_{Mn}/\mathbf{1}_{Ga}$ samples containing 10, 20, and 50% of $\mathbf{1}_{Mn}$ were prepared by mixing at the required ratio and coprecipitating CH_2Cl_2 solutions of $\mathbf{1}_{Mn}$ and $\mathbf{1}_{Ga}$ by a ca. 15-fold excess of n-hexane under vigorous stirring. Single crystals of $\mathbf{1}_{Mn}$ and $\mathbf{1}_{Mn}/\mathbf{1}_{Ga}$ were obtained by employing the layering method and CH_2Cl_2/n-hexane (1:4) as the solvent system.

Elemental Analysis of Mn and Ga. The Mn and Ga contents of the magnetically diluted samples were determined by microwave plasma atomic emission spectrometry (MP-AES). An Agilent 4210 MP-AES device (Agilent, Santa Clara, CA), equipped with an Inert One Neb nebulizer and a double-pass glass cyclonic spray chamber, was employed. For this purpose, 20 mg of each of the magnetically diluted systems $\mathbf{1}_{Mn}/\mathbf{1}_{Ga}$ were mixed with 5 mL of 65% (w/w) HNO_3(aq) (Suprapur, Merck Millipore), and the mixture was heated until complete digestion. The clear solution was transferred into a 50.00 mL volumetric flask and diluted with Millipore water. The measurements were carried out on samples taken from this solution. The instrumental/measurement parameters (Table S1) and the results (Table S2) are provided.

sH of $S = 2$ Systems. The zfs, expressed in terms of the axial-component D tensor, is the leading sH parameter for systems with a spin ground state $S \geq 1$.[77] The zfs describes lifting of the degeneracy of the $2S + 1$ magnetic sublevels $M_S = S, S - 1, ..., -S$, which, in the absence of an external magnetic field, are exactly degenerate at the level of the Born−Oppenheimer Hamiltonian. To first order in perturbation theory, the zfs arises from the direct magnetic-dipole spin−spin interaction between unpaired electrons (spin−spin coupling, SSC). To second order, the contributions arise from the spin−orbit coupling (SOC) between electronically excited states and the ground state. In order to describe the magnetic and EPR properties of an $S = 2$ system in perfect or near O_h symmetry, for the zfs terms, spin operators up to fourth order ($n = 4$) need to be considered, besides the electron and nuclear Zeeman and electron−nuclear hyperfine interactions. Collectively, these interactions are presented in the sH shown in eq 1:

$$H = \beta B\mathbf{g}S + D[S_z^2 - S(S+1)/3] + E(S_x^2 - S_y^2) + B_4^0 O_4^0 + B_4^2 O_4^2 + B_4^4 O_4^4 + I\mathbf{A}S - g_n\beta_n BI \quad (1)$$

in which β is the Bohr magneton, B is the magnetic field, $\mathbf{g}$ is a tensor, D and E are the axial and rhombic second-order zfs terms, respectively, O_4^m are the fourth-order zfs operators (Stevens operators), B_4^m are the fourth-order zfs parameters, and $\mathbf{A}$ is the hyperfine interaction tensor between the electronic spin of the $S = 2$ complex and the nuclear spin of the $I = {}^5/_2$ ^{55}Mn nucleus.[49] The higher-order terms of the zfs can be derived using group theoretical arguments for perfectly cubic systems.[78] The last term of eq 1 represents the nuclear Zeeman term, which is usually neglected.

Magnetometry. ac magnetometry experiments were carried out on a Quantum Design PPMS magnetometer, using an oscillating magnetic field (H_{ac}) of 10^{-4} T (1.0 Oe). Magnetization hysteresis loops on single crystals of $\mathbf{1}_{Mn}$ and 10% $\mathbf{1}_{Mn}/\mathbf{1}_{Ga}$ were measured by employing a micro-SQUID instrument in the temperature ranges of 0.03−5.0 and 0.03−1.1 K, respectively, and at field sweep rates varying in the range of 0.004−0.280 T s^{-1}.[79,80]

EPR Spectroscopy. *HFEPR.* HFEPR spectra were recorded using a spectrometer based on a 15/17 T superconducting magnet, differing from that already described[81] only by the use of a Virginia Diodes Inc. source operating at a base frequency of 12−14 GHz and increased by a cascade of multipliers. Alternatively, a backward-wave oscillator was used as a source of the highest frequencies (600−700 GHz). The spectra and their frequency dependencies were simulated using the software *SPIN* from Dr. A. Ozarowski (NHMFL).

Dual-Mode X-Band EPR. Dual-mode X-band EPR measurements were carried out on an upgraded Bruker ER-200D spectrometer equipped with an Oxford ESR 900 cryostat, an Anritsu MF76A

https://dx.doi.org/10.1021/acs.inorgchem.0c01636
Inorg. Chem. 2020, 59, 13281−13294

frequency counter, and a Bruker 035 M NMR gaussmeter. Either the perpendicular-mode standard cavity 4102ST or the dual-mode cavity 4116DM was used, which allows EPR to be run with the microwave magnetic field $\mathbf{B}_1$ oscillating perpendicular or parallel to the external magnetic field $\mathbf{B}$, respectively. The spectra were simulated by using the *SpinCount* package (Prof. M. P. Hendrich, Carnegie Mellon University).

Computational Details. All calculations were carried out using the *ORCA 4.0*[82] quantum chemistry computational package. Geometry optimization and frequency calculations were done by employing the BP86 functional,[83,84] the Ahlrichs polarized basis set def2-TZVP,[85−87] and Grimme's dispersion correction D3.[88,89] The resolution-of-identity approximation was employed with the auxiliary basis set def2-TZVP/J in order to speed up the calculations.[90] The sH parameters were computed using the state-averaged complete-active-space self-consistent field (SA-CASSCF)[91,92] in conjunction with the N-electron valence perturbation theory to second order (NEVPT2)[93,94] and spectroscopic oriented configuration interaction (SORCI)[95] in an effort to recover the missing dynamical correlation. The segmented all-electron relativistically contracted version[96] of Ahlrichs polarized basis set def2-TZVP[85−87] and the second-order Douglas−Kroll−Hess[97] (DKH) relativistic Hamiltonian were employed to account for the scalar relativistic effects. The active space was chosen to contain four electrons in five Mn 3d-based molecular orbitals (MOs). All states arising from the d^4 configuration (5 quintets, 30 triplets, and 10 singlets) were taken into account. SOC along with the Zeeman interaction can be introduced in the framework of quasi-degenerate perturbation theory (QDPT). In the QDPT scheme, SOC and Zeeman interactions act as a perturbation to the nonrelativistic Hamiltonian.[98] In this approach, the SOC operator is approximated by the spin−orbit mean-field (SOMF) operator,[98] which is an effective one-electron operator that contains one- and two-electron SOC integrals and also incorporates the spin−other orbit interaction. The SOC was treated using SOMF,[99] as implemented in *ORCA*. The second-order contributions to the $\mathbf{g}$ tensor, zfs, and hyperfine coupling constant (hfcc) sH parameters were computed in the framework of the effective Hamiltonian approach[100,101] as well as the sum over states (SOS) approach.[102,103] The Fermi contact (FC) and spin dipolar (SD) were computed in the framework of linear-response (LR) theory,[104] where the involved unrelaxed response spin densities are computed by employing the domain local pair natural orbital couple cluster singles and doubles (DLPNO−CCSD) level of theory.[105,106] For these calculations, deconstructed versions of the above basis sets were used.

RESULTS AND DISCUSSION

Molecular Structure. The molecular structure of $\mathbf{1}_{\mathbf{Mn}}$ is shown in Figure 1.[28,41] The MnO_6 core of **1** exhibits an elongated octahedral geometry, due to Jahn−Teller distortion, with average axial and equatorial Mn−O bond distances of 2.159 and 1.933 Å, respectively.[28] Additional distortions to the MnO_6 core are imposed by the second coordination sphere involving the 12 phenyl rings of the three chelating ligands.[107] This is reflected in the magnitude of the axial and equatorial O−Mn−O angles, which deviate from linearity by 2−5°. As a result, the local symmetry of the MnO_6 core is lower than D_{4h}. This lowering of symmetry is expected to affect the magnitude of the D, E, and higher-order zfs terms, which control the magnetization relaxation of complex $\mathbf{1}_{\mathbf{Mn}}$.

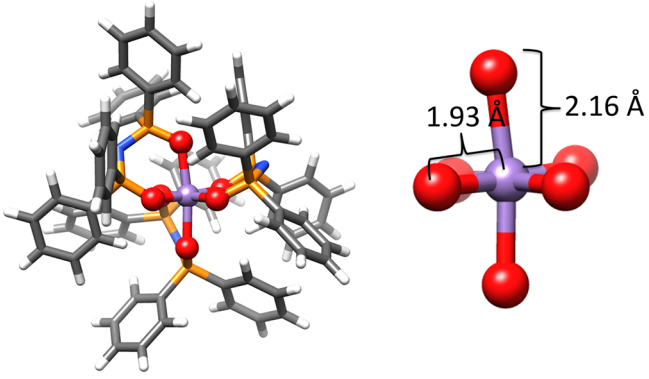

Figure 1. Molecular structure of $\mathbf{1}_{\mathbf{Mn}}$.[28,41] Color code: Mn, purple; O, red; P, orange; N, blue; C, gray; H, white.

Quantification of the Mn and Ga Contents. The Mn contents of the nominally 10, 20, and 50% magnetically diluted $\mathbf{1}_{\mathbf{Mn}}/\mathbf{1}_{\mathbf{Ga}}$ systems were determined to be 8.7 ± 0.6, 19.6 ± 0.8, and 44.8 ± 0.8%, respectively, by MP-AES (Table S2).

ac Magnetometry. In most of the 3d-based SIMs, application of an external dc magnetic field is needed to induce slow magnetic relaxation,[21] except for some interesting exceptions of Fe(I), Fe(III), and Co(II) complexes.[22] Field-induced slow magnetic relaxation of powdered samples of $\mathbf{1}_{\mathbf{Mn}}$ has already been probed by means of ac magnetometry.[28] These observations prompted us to study the magnetic behavior of magnetically diluted $\mathbf{1}_{\mathbf{Mn}}/\mathbf{1}_{\mathbf{Ga}}$ samples containing 20 or 50% $\mathbf{1}_{\mathbf{Mn}}$. Magnetic dilution has been employed to probe possible intermolecular interactions in slow-relaxing systems, such as Co(II),[108−110] Ni(II),[111] and U(III)[112] complexes. To the best of our knowledge, this is the first report of the effects of magnetic dilution on the relaxation properties of mononuclear Mn(III) complexes. The χT product of the 20 and 50% $\mathbf{1}_{\mathbf{Mn}}/\mathbf{1}_{\mathbf{Ga}}$ at $T > 30$ K amounts to 4.94×10^{-4} and 1.10×10^{-3} cm^3 g^{-1} K, respectively. These values correspond to ∼22 and 48% of the value for complex $\mathbf{1}_{\mathbf{Mn}}$ (2.30×10^{-3} cm^3 g^{-1} K)[28] and are in reasonable agreement with the Mn content of the corresponding $\mathbf{1}_{\mathbf{Mn}}/\mathbf{1}_{\mathbf{Ga}}$ systems, as determined by MP-AES (vide supra; Table S2).

The spin-relaxation properties of the magnetically diluted $\mathbf{1}_{\mathbf{Mn}}/\mathbf{1}_{\mathbf{Ga}}$ samples were monitored by ac magnetometry, either in the absence or in the presence of a dc magnetic field. As was also the case for complex $\mathbf{1}_{\mathbf{Mn}}$,[28] no out-of-phase signals were observed in the absence of an external magnetic field. However, slow relaxation was induced in the presence of external magnetic fields (Figures 2 and S1). Similar with

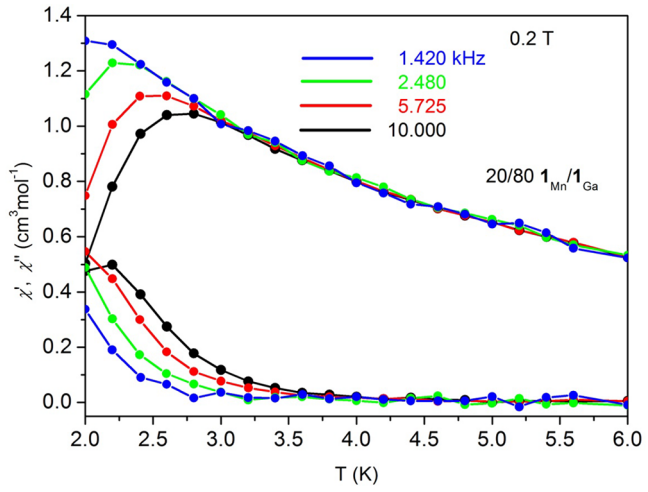

Figure 2. Temperature and frequency dependence of the real (χ'; top curves) and imaginary (χ''; bottom curves) parts of the magnetic susceptibility of 20% $\mathbf{1}_{\mathbf{Mn}}/\mathbf{1}_{\mathbf{Ga}}$ in the presence of a dc field of 0.2 T. Solid lines are guides to the eye.

https://dx.doi.org/10.1021/acs.inorgchem.0c01636
Inorg. Chem. 2020, 59, 13281−13294

complex $\mathbf{1}_{Mn}$, no maximum was observed for χ'' down to 2 K (Figures 2 and S1), which is the lowest temperature of our experimental setup for both $\mathbf{1}_{Mn}$ and $\mathbf{1}_{Mn}/\mathbf{1}_{Ga}$. Because of this, it was not possible to determine accurately the relaxation time and its exact temperature dependence. An estimate may be provided by examining the dependence of the quantity $\ln(\chi''/\chi')$ as a function of $1/T$ for various values of the external dc magnetic field. In Figures 3 and S2, representative plots are

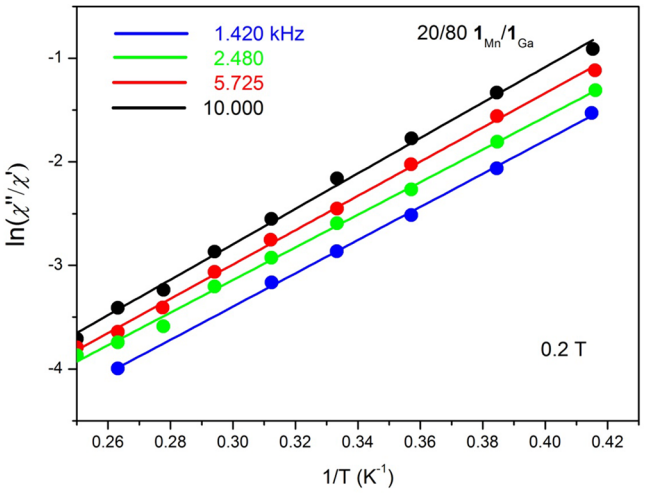

Figure 3. $\ln(\chi''/\chi')$ versus $1/T$ plots for 20% $\mathbf{1}_{Mn}/\mathbf{1}_{Ga}$ in the presence of a dc field of 0.2 T. Solid lines are fits obtained by eq 2.

shown, on the basis of data obtained at a magnetic field of 0.2 T for 20 and 50% $\mathbf{1}_{Mn}/\mathbf{1}_{Ga}$, respectively. Similar plots obtained at different dc magnetic fields are shown in Figures S3–S14. These studies revealed that $\ln(\chi''/\chi')$ depends almost linearly on $1/T$ in the 2.4–3.5 K temperature range. As in our previous report,[28] the data were analyzed by using eq 2:[113]

$$\ln(\chi''/\chi') = \ln(2\pi\nu\tau_0) + \Delta/k_bT \quad (2)$$

From analysis of the experimental data on the basis of eq 2 for various values of an external magnetic field, the values for τ_0 and Δ were obtained and are listed in Table S3. The preexponential factors τ_0 of 50 and 20% $\mathbf{1}_{Mn}/\mathbf{1}_{Ga}$ amount to $(1.1–2.7) \times 10^{-8}$ and $(0.8–2.0) \times 10^{-8}$ s, respectively. Correspondingly, the magnitudes of the thermal barrier Δ are 10.3(6) and 11.6(2) cm^{-1}, respectively. The values of the preexponential factor and thermal barrier Δ are similar to the values determined for $\mathbf{1}_{Mn}$[28] (Table S3). The studies presented herein demonstrate that the magnetically diluted $\mathbf{1}_{Mn}/\mathbf{1}_{Ga}$ systems exhibit magnetic relaxation properties similar to those of the undiluted complex. This finding provides compelling evidence that the magnetic relaxation behavior of $\mathbf{1}_{Mn}$ is governed by the intrinsic properties of the individual molecules of $\mathbf{1}_{Mn}$ and not by intermolecular magnetic interactions.

Single-Crystal Micro-SQUID Studies. In order to gain further insight into the low-temperature slow magnetic relaxation behavior, single-crystal magnetic studies on $\mathbf{1}_{Mn}$ and 10% $\mathbf{1}_{Mn}/\mathbf{1}_{Ga}$ were performed using a micro-SQUID instrument. Magnetization (M) versus magnetic field plots are shown in Figures 4 and S15, respectively. Hysteresis loops were observed below 1 K, which became more pronounced with increasing sweep rate and decreasing temperature. However, the loop at 0.03 K was smaller than those at 0.1–

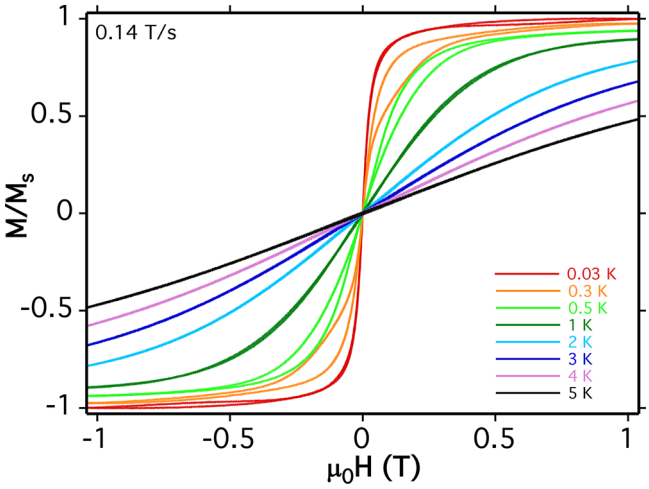

Figure 4. Field dependence of the normalized magnetization of $\mathbf{1}_{Mn}$ in the temperature range 0.03–5 K at field sweep rate of 0.14 T s^{-1}.

0.5 K. Similar phenomena have been observed for other Co(II)[114–116] and Mn(III)[27]-based SIMs, which are due to the effect of the high tunneling rate at 0.03 K. Besides, the observed closed hysteresis loop at zero dc field could be attributed to fast quantum tunneling of magnetization. This is consistent with the ac magnetic susceptibility measurements (vide supra). It has been shown that this behavior is attributed to direct spin transitions between the magnetic sublevels $|S, M_S\rangle$[117] that have been reported for other mononuclear Mn(III) complexes.[27] In the following Quantum-Chemical Calculations section Magnetic Sublevels Analysis and Selection Rules, this phenomenon will be further discussed (vide infra).

In the micro-SQUID experiment, the magnetic field was aligned with the mean easy axis of magnetization using the transverse field method, as previously described,[118] which allowed us to confirm that the zfs parameter D of $\mathbf{1}_{Mn}$ is negative.

HFEPR Spectroscopy. The $S = 2$ complex $\mathbf{1}_{Mn}$ was previously studied by dc magnetometry, which provided an estimate of the sH parameters g and D. In addition, simulations of parallel-mode X-band EPR spectra of complex $\mathbf{1}_{Mn}$ revealed an involvement of E and/or fourth-order zfs terms, but their relative contributions were not conclusively established.[28] To this end, complex $\mathbf{1}_{Mn}$ was studied by HFEPR spectroscopy within the current work in order to accurately determine its sH parameters.

Technical details concerning the sample preparation and acquisition of HFEPR spectra are presented in the Supporting Information. Typical single-frequency HFEPR spectra of $\mathbf{1}_{Mn}$ are shown in Figures 5 and S16–S18. On the basis of these data, a standard field versus frequency two-dimensional map[119] was constructed. This is shown in Figure 6, in which the squares are experimental points, while the lines were drawn using best-fitted sH parameters including fourth-order zfs terms, as follows: $S = 2$, $|D| = 3.917(5)$ cm^{-1}, $|E| = 0.018(4)$ cm^{-1} ($E/D = 0.0046$), $B_4^0 = B_4^2 = 0$, $B_4^4 = (3.6 \pm 1.7) \times 10^{-3}$ cm^{-1}, and $\mathbf{g} = [1.994(5), 1.996(4), 1.985(4)]$. The inclusion of the finite fourth-order zfs parameter B_4^4 noticeably improved the fit quality.

The accuracy of the sH parameters was confirmed by simulating single-frequency spectra (Figures 5 and S17 and S18). This endeavor also allowed us to unequivocally determine the sign of D. While the spectra at moderate

https://dx.doi.org/10.1021/acs.inorgchem.0c01636
Inorg. Chem. 2020, 59, 13281–13294

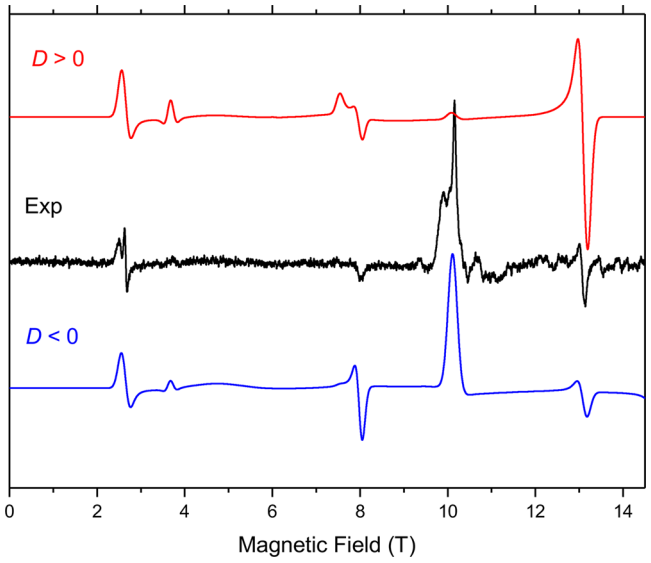

Figure 5. HFEPR spectrum of a pellet of complex $\mathbf{1}_{Mn}$ obtained at 10 K and 633 GHz (black trace) accompanied by its simulations using the sH parameters listed in the text. The red trace represents positive D and the blue trace negative D. The parameter E was assigned the same sign as D, by convention. The apparent doubling of the 2.5 and 10.2 T turning points is a result of a residual torqueing effect not fully prevented by pressing a pellet (Figure S16).

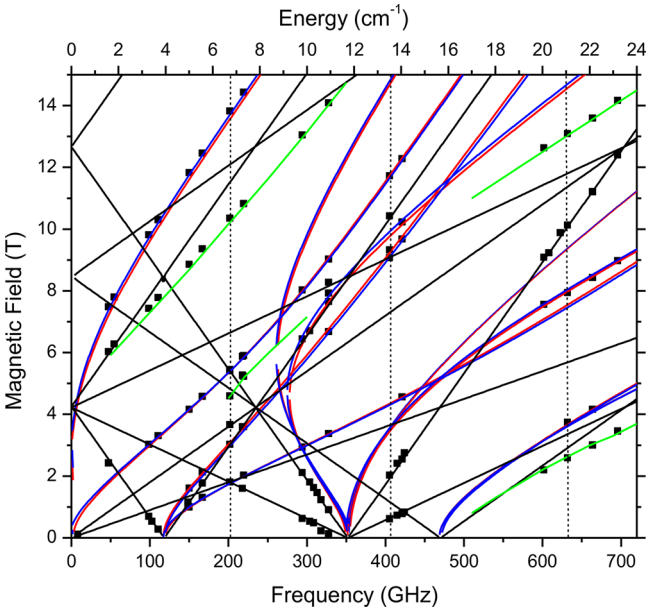

Figure 6. Two-dimensional magnetic field versus frequency map of resonances for complex $\mathbf{1}_{Mn}$. The squares are experimental points, while the lines were drawn using the best-fitted sH parameters, as listed in the text. Red lines: turning points with $B_0 \| x$. Blue lines: $B_0 \| y$. Black lines: $B_0 \| z$. Green lines: off-axis turning points. The parallel-mode resonance obtained at the X-band[28] is included in the map at 9.3 GHz. The three dashed vertical lines represent the frequencies at which spectra shown in Figures S17 and S18 and 5, in increasing order, were recorded.

frequency (203 GHz, Figure S17) still show some ambiguity in this respect, those recorded at 406 and 633 GHz (Figures S18 and 5, respectively) leave no doubt about the negative sign of D. This finding confirms the fact that tetragonally-elongated (due to Jahn–Teller distortion effects) Mn(III) complexes exhibit negative D.[51] The notable exception of the Mn(III) complex $[Mn(cyclam)I_2]I$ (cyclam = 1,4,8,11-tetraazacyclotetradecane), which exhibits a positive D despite being tetragonally elongated, was attributed to significant SOC effects of its heavy I^- ligand.[70]

Dual-Mode X-Band EPR Spectroscopy. At X-band EPR of an $S = 2$ spin state, the observed transitions arise from the $|M_S\rangle = |\pm 2\rangle$ quasi-doublet. In order for such transitions to be observed, mixing between the $|-2\rangle$ and $|+2\rangle$ spin sublevels is required. This mixing can occur through the rhombic second-order term E and/or the fourth-order zfs terms. Because both terms result in similar effects (see the related analysis in the Supporting Information), X-band spectra alone cannot unequivocally distinguish the relative contribution of each parameter. X-band EPR spectra can be used to quantitatively determine the contribution of the fourth-order terms, provided that the contribution of the other terms had been previously determined by analysis of the HFEPR spectra.[59] In previous work reported by some of us, the parallel-mode X-band EPR spectra of $\mathbf{1}_{Mn}$ were simulated by considering an $|E|$ value of 0.387 cm^{-1} and neglecting the fourth-order terms.[28] However, the HFEPR studies reported herein clearly indicate that E is smaller by a factor of 20 (0.018 cm^{-1}), and using this value and ignoring fourth-order terms, the X-band EPR spectra cannot be reproduced even approximately. In particular, the simulated position of the resonance corresponds to a smaller g_{eff} value (very close to the value of $4g_z$) than the one observed. In addition, at this limit, the resonance involves a transition between almost pure $|-2\rangle$ and $|+2\rangle$ spin sublevels and the transition probability is prohibitively low, rendering them practically unobservable with our setup (see the related analysis in the Supporting Information). Inevitably, fourth-order zfs terms need to be incorporated in the sH. From the HFEPR spectra, the parameters D and E and the $\mathbf{g}$ tensor were determined with great accuracy. In addition, out of the three fourth-order zfs terms, only B_4^4 was shown to contribute. On the basis of these findings, subsequent analysis of the parallel-mode X-band EPR spectra provided A_z and the fourth-order parameter B_4^4. The spectrum of the complex $\mathbf{1}_{Mn}$ was simulated (Figure 7A) by assuming A_z = 155 MHz and $B_4^4 = 4.2(2) \times 10^{-3}$ cm^{-1} (Table S4). The value of B_4^4 agrees well with that determined (albeit less precisely) by HFEPR and is of the same order of magnitude as that observed for other mononuclear $S = 2$ Mn(III) complexes.[27,48,57,59,63,65] Similarly, the A_z value is consistent with a tetragonally elongated Mn(III) octahedral coordination sphere exhibiting a $^5B_{1g}$ electronic ground state (vide infra).[65,120−122]

The specific line shape of the parallel-mode signal is determined by the hyperfine interactions. However, no hyperfine lines were resolved in the 4.2 K spectrum of complex $\mathbf{1}_{Mn}$[28] (Figure 7A) because of broadening mechanisms that smear them out. These broadening mechanisms may involve distributions in the zfs parameters and/or intermolecular interactions in the solid state. In Figure 7B, the 4.2 K parallel-mode X-band EPR spectrum of 20% $\mathbf{1}_{Mn}/\mathbf{1}_{Ga}$ is shown. Importantly, the dilution at this level increased the resolution of the hyperfine lines. The line shape can be modeled by changing the intrinsic line widths in the simulations. For the spectrum shown in Figure 7A, the intrinsic line width used was 3.0 mT, whereas for the spectrum shown in Figure 7B, the intrinsic line width was 2.0 mT. These data indicate that the broadening mechanism involves weak intermolecular interactions, either through static dipolar

https://dx.doi.org/10.1021/acs.inorgchem.0c01636
Inorg. Chem. 2020, 59, 13281−13294

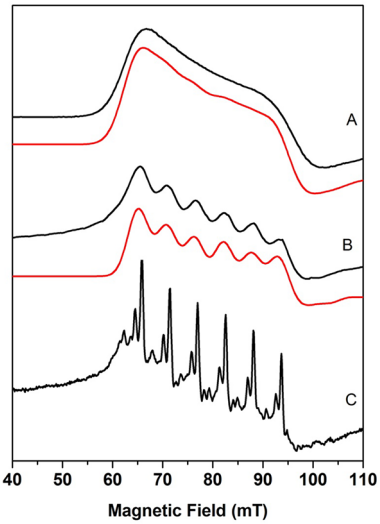

Figure 7. Parallel-mode X-band EPR at 4.2 K of powdered samples of $\mathbf{1}_{Mn}$ (A), magnetically diluted sample 20% $\mathbf{1}_{Mn}/\mathbf{1}_{Ga}$ (B), and a frozen solution of $\mathbf{1}_{Mn}$ in CH_2Cl_2 (C). EPR conditions: modulation amplitude, 0.1 mT_{pp} (A and B) and 0.5 mT_{pp} (C); microwave power, 2.0 mW; microwave frequency, 9.3 GHz. The perpendicular-mode X-band spectra are shown in Figure S19.

interactions or spin relaxation that affects the intrinsic line width of the transitions. These interactions are much weaker than those required to affect the ac magnetometry measurements presented above. Magnetic dilution reduces these interactions, and the hyperfine lines are better resolved.

Ideally, good isolation between molecules can be achieved also in solution. A spectrum of a frozen CH_2Cl_2 solution of $\mathbf{1}_{Mn}$ at ca. 4 mM concentration is shown in Figure 7C. The spectrum comprises impressively narrow lines (full width at half-maximum, ~0.6 mT) superimposed on a broad background. Narrow lines in parallel-mode X-band EPR spectra of frozen solutions of Mn(III) complexes are not unprecedented in the literature,[44,65,121−123] but in the present case, the narrowness of the lines allows for the resolution of additional subtler features. Apart from the dominating strong sextet, additional lines can be readily recognized. Overall, the lines of the spectrum can be grouped in four sextets and represent S = 2 Mn(III) species of slightly different conformations, exhibiting different zfs parameters. In order to keep the number of variables as small as possible, we assumed that the four sites are characterized by the same D, E, and g_z (determined for the powder samples of $\mathbf{1}_{Mn}$) and we vary A_z and B_4^4. The spectra can be reproduced with the parameters listed in Table S4. The positions of the lines of the four sextets are shown by the colored stick diagrams in Figure S20. In addition, analysis yielded the relative abundance of these different species. The majority species account for ~80% of the S = 2 sites and are characterized by the smallest B_4^4 parameter. The minority species represent a rather small fraction of the centers and are characterized by larger values of the B_4^4 parameter. Despite their small abundance, the presence of the minority species can be manifested and quantified in the spectra because the transition probability increases significantly as B_4^4 increases (see the related analysis in the Supporting Information). The extremely narrow line widths indicate a well-defined environment for each species. In the powder samples, the existence of distinct species cannot be revealed in the spectra and the main broadening mechanism involves intermolecular interactions. Up to now, the full ^{55}Mn(III) hyperfine coupling tensor with its orientation has been determined only for magnetically diluted $[Mn(H_2O)_6]^{3+}$.[48,65] The work presented herein provides additional data of hyperfine coupling in both solution and the solid state of an S = 2 Mn(III) complex, which serve as computational benchmark values (vide infra).

Quantum-Chemical Calculations. *Electronic Structure.* Complex $\mathbf{1}_{Mn}$ containing an approximate D_{4h} MnO_6 first coordination sphere exhibits a $^5B_{1g}$ ground state of the electron configuration $e_g(d_{xz/yz})^2b_{2g}(d_{xy})^1a_{1g}(d_{z^2})^1b_{1g}(d_{x^2-y^2})^0$. The important single-electron excitations, depicted in Figure 8, are of

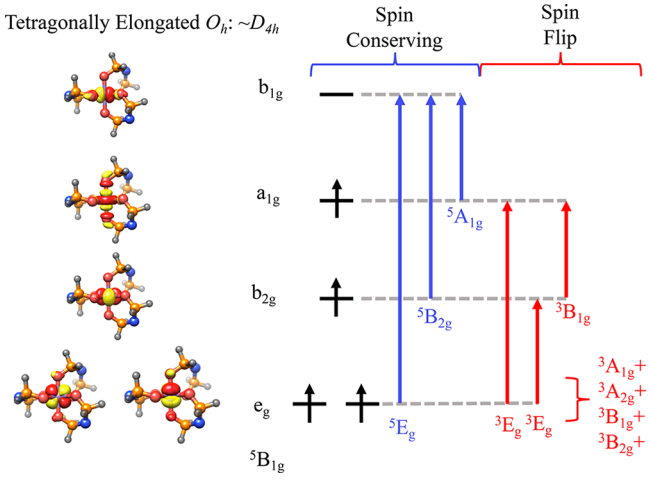

Figure 8. Metal d-based molecular orbitals and term symbols arising from single-electron excitations for $\mathbf{1}_{Mn}$. The indicated orbital occupation pattern refers to the $^5B_{1g}$ ground state.

spin-conserving and spin-flip character. Spin-conserving excitations arise from the singly occupied molecular orbitals (SOMOs) to the $d_{x^2-y^2}$ (b_{1g}) virtual molecular orbital (VMO), namely, $^5A_{1g}(d_{z^2}\rightarrow d_{x2-y2})$, $^5B_{2g}(d_{xy}\rightarrow d_{x2-y2})$, and $^5E_g(d_{xz/yz}\rightarrow d_{x2-y2})$. By contrast, spin-flip excitations arise from single excitations within the SOMOs, namely, $^3B_{1g}(d_{xy}\rightarrow d_{z^2})$, $^3E_g(d_{xz/yz}\rightarrow d_{z^2})$, $^3E_g(d_{xz/yz}\rightarrow d_{xy})$, and $^3A_{1g}$, $^3A_{2g}$, $^3B_{1g}$, and $^3B_{2g}(d_{xz/yz}\rightarrow d_{xz/yz})$.

g Values. The g values were computed on the basis of the effective Hamiltonian approach,[101] in the framework of SA-CASSCF/NEVPT2 and SA-CASSCF/SORCI calculations. The SA-CASSCF/NEVPT2 calculations were performed on the full structure of $\mathbf{1}_{Mn}$,[28,41] while the SA-CASSCF/SORCI calculations were performed on a truncated model, $^H\mathbf{1}_{Mn}$, in which the phenyl groups were replaced by hydrogen atoms. As shown in Table 1, all g values are in good agreement with those determined by the HFEPR measurements (vide supra), reflecting the tetragonally-elongated Mn(III) coordination

Table 1. Calculated g-Tensor Parameters for the Complex $\mathbf{1}_{Mn}$ and Model $^H\mathbf{1}_{Mn}$

model	method	g_x	g_y	g_z
$\mathbf{1}_{Mn}$	CASSCF	1.997	1.997	1.995
	NEVPT2	1.997	1.998	1.996
$^H\mathbf{1}_{Mn}$	CASSCF	1.996	1.996	1.993
	NEVPT2	1.997	1.998	1.995
	SORCI	1.998	1.999	1.997

https://dx.doi.org/10.1021/acs.inorgchem.0c01636
Inorg. Chem. 2020, 59, 13281−13294

Table 2. Calculated zfs Parameters for the Complex $\mathbf{1}_{Mn}$ and Model $^{H}\mathbf{1}_{Mn}$

model	method	D^{SSC} (cm^{-1})	D^{SOC} (cm^{-1})	E/D	B_4^0 ($\times10^{-3}$ cm^{-1})	B_4^2 ($\times10^{-3}$ cm^{-1})	B_4^4 ($\times10^{-3}$ cm^{-1})
$\mathbf{1}_{Mn}$	CASSCF	−0.41	−3.35	0.01	0.001	0.001	2.3
	NEVPT2	−0.42	−3.12	0.01	0.001	0.001	1.8
$^{H}\mathbf{1}_{Mn}$	CASSCF	−0.43	−3.45	0.01	0.001	0.001	2.6
	NEVPT2	−0.44	−3.10	0.01	0.001	0.001	1.6
	SORCI	−0.45	−3.21	0.01	0.001	0.001	2.1

environment. In particular, all g values are smaller than 2.0, which is consistent with the less than half-filled d^4 electronic configuration of Mn(III). In fact, the main contribution to the computed g values is due to the SOMO−VMO single-electron excitations.[124] In particular, quintet states that are dominated by the z-polarized $^5A_{1g}(d_{z^2}\rightarrow d_{x^2-y^2})$ electron excitation and the xy- and z-polarized $^5B_{2g}(d_{xy}\rightarrow d_{x^2-y^2})$ and $^5E_g(d_{xy/yz}\rightarrow d_{x^2-y^2})$ electron excitations provide the major contributions to the g_z and g_{xy} values, respectively.

zfs. For calculation of the zfs parameters, the effective Hamiltonian approach[101] was similarly employed in the framework of SA-CASSCF/NEVPT2 and SA-CASSCF/SORCI calculations on the full structure of $\mathbf{1}_{Mn}$[28,41] and the truncated model $^{H}\mathbf{1}_{Mn}$, respectively. It should be mentioned that, as has been shown repeatedly in the concept of the above employed ab initio wave function computational protocols, the many-particle states are treated to infinite order.[23,107,117,125] Hence, it is possible to extract the predominant contributions to the zfs. The results, listed in Table 2, show that in all cases the second-order contributions (D^{SOC}) are negative. Analysis of the data shows that the spin-conserving and spin-flip excitations contribute to D^{SOC} by 35% $^5B_{2g}(d_{xy}\rightarrow d_{x^2-y^2})$, 15% $^5E_g(d_{xz/yz}\rightarrow d_{x^2-y^2})$, and 50% $^3B_{1g}(d_{xy}\rightarrow d_{z^2})$, respectively. According to the SA-CASSCF/NEVPT2 and SA-CASSCF/SORCI calculations, the first-order contributions (D^{SSC}) are about 10% of the respective second-order contributions, which is consistent with the findings of reported studies on other octahedral Mn(III) complexes.[126,127] On the basis of the SA-CASSCF/NEVPT2 and the SA-CASSCF/SORCI calculations, the calculated $|D|$ (D^{SSC} + D^{SOC}) parameter ranges between 3.60 and 3.80 cm^{-1}, with E/D being equal to 0.01. These results are in good agreement with the data obtained by HFEPR (vide supra).

In a second step, the calculated model interaction matrix of the effective Hamiltonian was mapped by using the following model Hamiltonian:

$\hat{H}_{Model}$	$\|2,-2\rangle$	$\|2,-1\rangle$	$\|2,0\rangle$	$\|2,+1\rangle$	$\|2,+2\rangle$
$\langle 2,-2\|$	$4D-60B_4^0$	0	$\sqrt{6}D+3\sqrt{6}B_4^2$	0	$12B_4^4$
$\langle 2,-1\|$	0	$D-120B_4^0$	0	$3E-12B_4^2$	0
$\langle 2,0\|$	$\sqrt{6}D+3\sqrt{6}B_4^2$	0	0	0	$\sqrt{6}D+3\sqrt{6}B_4^2$
$\langle 2,+1\|$	0	$3E-12B_4^2$	0	$D-120B_4^0$	0
$\langle 2,+2\|$	$12B_4^4$	0	$\sqrt{6}D+3\sqrt{6}B_4^2$	0	$4D-60B_4^0$

It has been shown that, in this way, information with respect to the higher than second-order zfs terms B_4^0, B_4^2, and B_4^4, can be obtained.[128] The data listed in Table 2 show that, in all cases, the B_4^0 and B_4^2 terms are negligible ($<10^{-6}$ cm^{-1}) and the main contributions (1.6−2.6) × 10^{-3} cm^{-1} arise from the B_4^4 terms. These values are also consistent with the EPR experimental observations (vide supra), as well as with previously reported experimental and computational studies.[101,128]

hfcc Values. Hyperfine interaction contains three contributions of different physical origins, namely, the isotropic Fermi contact term (A^{FC}), the traceless spin-dipolar term (A^{SD}), and the spin−orbit coupling term (A^{SOC}).[49] While A^{FC} and A^{SOC} are proportional to the spin population of the nucleus of interest (the Mn center) and the g values, A^{SD} can be thought of as a measure of the deviation of the spin density from the spherical symmetry. In the case of complex $\mathbf{1}_{Mn}$ and the truncated $^{H}\mathbf{1}_{Mn}$ model, the g values are essentially isotropic and close to the electron g value (∼2.0). This suggests that the conditions of quenched orbital angular momentum are met and, hence, the A^{SOC} contributions to the hfcc values are expected to be negligible.

The accuracy of the computed hfcc values is closely associated with accurate determination of the FC term (A^{FC}).[106,120,129−132] We have recently shown that, for a number of mononuclear complexes, accurate A^{FC} and A^{SD} can be obtained in the framework of LR theory,[104] where the involved unrelaxed response spin densities are computed by employing the DLPNO−CCSD level of theory.[105,106] Hence, in the following, the A^{FC} and A^{SD} values were computed at the DLPNO−CCSD level of theory, while the A^{SOC} values for $\mathbf{1}_{Mn}$ were estimated by CASSCF/NEVPT2 calculations by employing the effective Hamiltonian approach. On the other hand, the A^{SOC} values of $^{H}\mathbf{1}_{Mn}$ were estimated by SORCI calculations employing the SOS approach.

The ^{55}Mn hfcc values computed for the $\mathbf{1}_{Mn}$ and $^{H}\mathbf{1}_{Mn}$ systems are presented in Table 3. For $\mathbf{1}_{Mn}$ and $^{H}\mathbf{1}_{Mn}$, $A_{xy}(A_{xy}^{Total})$ ranges between −254 and −264 MHz, while $A_z(A_z^{Total})$ ranges between −154 and −158 MHz. The latter value is in very good agreement with the A_z value determined by parallel-mode EPR experiments (A_z = |155| MHz, vide supra). In general, these values are consistent with a Mn(III)

Table 3. Calculated hfcc x, y, and z Parameters (A^{Total}) for Complex $\mathbf{1}_{Mn}$ and the Truncated Model $^{H}\mathbf{1}_{Mn}$, together with the FC (A^{FC}), SD (A^{SD}), and SOC (A^{SOC}) Contributions

model	hfcc	x (MHz)	y (MHz)	z (MHz)
$\mathbf{1}_{Mn}$	A^{FC}[a]	−220	−220	−220
	A^{SD}[a]	−35	−35	72
	A^{SOC}[b]	−1	−1	−5
	A^{Total}	−254	−254	−154
$^{H}\mathbf{1}_{Mn}$	A^{FC}[a]	−230	−230	−230
	A^{SD}[a]	−33	−33	76
	A^{SOC}[c]	−1	−1	−5
	A^{Total}	−264	−264	−158

[a] A^{FC} and A^{SD} are estimated from DLPNO−CCSD computations for both $\mathbf{1}_{Mn}$ and the model $^{H}\mathbf{1}_{Mn}$. [b] In the case of $\mathbf{1}_{Mn}$, A^{SOC} is estimated from CASSCF/NEVPT2 calculations employing the effective Hamiltonian approach. [c] In the case of $^{H}\mathbf{1}_{Mn}$, A^{SOC} is estimated from SORCI calculations employing the SOS approach.

https://dx.doi.org/10.1021/acs.inorgchem.0c01636
Inorg. Chem. 2020, 59, 13281−13294

center in a tetragonally-elongated octahedral coordination environment.[44,46,65,120,133]

In a further step, the computed hfcc values were analyzed in terms of FC, SD, and SOC interactions. Analysis of the individual contributions reveals that, in both $^{1}\mathbf{Mn}$ and $^{H}\mathbf{1}_{\mathbf{Mn}}$, the FC term ($A^{FC}$) is predominant (>85%). By contrast, the SOC contribution to the hfcc values (A^{SOC}), as expected for an Mn(III) O_h center, is negligible (<1%). The SD part amounts to $A_{xy}^{SD} \sim -35$ MHz and $A_z^{SD} \sim 72$ MHz for $\mathbf{1}_{\mathbf{Mn}}$ and $A_{xy}^{SD} \sim -33$ MHz and $A_z^{SD} \sim 76$ MHz for $^{H}\mathbf{1}_{\mathbf{Mn}}$. In fact, because all g values are <2, A_z^{SD} and A_z^{SD} have different signs. Taking into account that $A^{FC} < 0$ and that A^{SOC} is negligible, the following relations apply: $A_{xy}^{SD} < 0$ and, hence, $A_{xy}^{Total} < A^{FC}$, while $A_z^{SD} > 0$ and, hence, $A_z^{Total} > A^{FC}$. As in many first-row transition mononuclear complexes,[44,46,102,120−122,133] one can conclude that the A^{Total} anisotropy is directly associated with the A^{SD} anisotropy arising from the asymmetry of the spin-density distribution in the singly occupied valence orbitals.

Magnetic Sublevels Analysis and Selection Rules. The magnetic relaxation properties of $\mathbf{1}_{\mathbf{Mn}}$ are discussed in both the framework of the sH and the many-particle-Hamiltonian approximations.

i. sH. Within the framework of the sH, the five magnetic sublevels $|\Psi_{0-4}\rangle$ that describe the physical system are a linear combination of the five $|M_S\rangle$ states. By using the zfs parameters determined experimentally on the basis of eq 1, the energies of the $|\Psi_{0-4}\rangle$ states, as well as the $|M_S\rangle$ compositions of the $|\Psi_{0-4}\rangle$ states, in the absence (Table S5) and in the presence of 0.1 T (Tables S6−S8) and 1.0 T (Tables S9−S11) external magnetic fields, are shown in the Supporting Information. The chosen magnetic field values are indicative; the 0.1−1.0 T field range corresponds to the field values used to probe the magnetic relaxation in the ac susceptibility measurements. Moreover, the 0.1 T value is close to the value of the magnetic field where the parallel-mode EPR signal is observed at the X-band. In the presence of a magnetic field, the wave functions are listed along the principal x, y, and z axes. As can be seen, at 0 T the compositions of states $|\Psi_{0,1}\rangle$, $|\Psi_{2,3}\rangle$, and $|\Psi_4\rangle$ amount to $|\pm2\rangle$, $|\pm1\rangle$, and $|0\rangle$ M_S states, respectively. Along the z axis, the state splitting amounts to 0.38 cm^{-1} (on the order of the microwave energy at the X-band) at 0.1 T and reaches a value of 3.7 cm^{-1} at 1 T. At this field, the composition of states $|\Psi_{0-4}\rangle$ contains pure (>99%) contributions from the $|-2\rangle$, $|+2\rangle$, $|-1\rangle$, $|+1\rangle$, and $|0\rangle$ M_S states.

The magnetic relaxation phenomenon is associated with the transitions between the $|\Psi_{0-4}\rangle$ states. These transitions occur for nonzero values of the quantity $TP_{ij,x,y,z} = \beta^2|\langle\psi_i|g_{x,y,z}S_{x,y,z}|\psi_j\rangle|^2$ (i = 0−4).[49] By using the values listed in Tables S5−S11, the quantities $TP_{0j,x}$, $TP_{0j,y}$, and $TP_{0j,z}$ and the average $TP_{0j} = (TP_{0j,x} + TP_{0j,y} + TP_{0j,z})/3$ for the transitions between the $|\Psi_0\rangle$ and $|\Psi_{1-4}\rangle$ states can be calculated and are listed in Table S12. The $|\Psi_0\rangle \rightarrow |\Psi_1\rangle$ transition corresponds essentially to spin reversal (from $M_S = -2$ to +2). The dependence of the probability for this particular transition on the magnetic field is illustrated in Figure 9. At 0 T, the transition probability is large and, hence, results in fast relaxation. This explains the fast relaxation observed in the ac susceptibility measurements and the closed hysteresis loops at 0 T. At 0.1 T, TP_{01} is almost 20 times smaller, and, consequently, the relaxation involving these two states will become progressively blocked. However, $TP_{01,z}$ is not negligible, and the transition is still partially allowed. This transition is observed by parallel-mode EPR spectroscopy at the X-band. For higher magnetic fields, this transition is

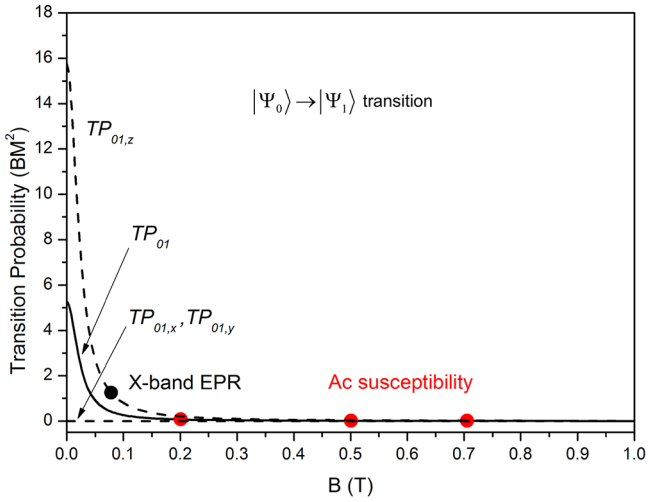

Figure 9. Dependence of the transition probabilities $TP_{01,x}$, $TP_{01,y}$, $TP_{01,z}$, and TP_{01} for the $|\Psi_0\rangle \rightarrow |\Psi_1\rangle$ transition on the magnetic field. Closed symbols indicate the values of the magnetic field at which the parallel-mode X-band EPR signal is observed and the dc magnetic fields used to carry out the ac susceptibility measurements.

practically forbidden (at 1.0 T, $TP_{01,z}$ is 2000 times smaller than that at 0 T) and relaxation through the $|\Psi_0\rangle \rightarrow |\Psi_1\rangle$ transition is blocked. Therefore, relaxation has to proceed through excited states (namely, $|\Psi_0\rangle \rightarrow |\Psi_2\rangle$, etc.), resulting in a thermally-activated process, as observed by the ac susceptibility measurements.

ii. Many-Particle-Hamiltonian Approximation. As shown above, the X-band EPR spectra arise mainly from the spin sublevel $|\pm2\rangle$. This is, however, a nominally forbidden magnetic-dipole transition ($\Delta M_S = \pm4$) and can only occur upon mixing of the magnetic sublevels due to the action of E and/or the higher than second-order zfs terms. It should be emphasized that state mixing implies that M_S is not a good quantum number anymore, and it is practically unable to describe the relativistically corrected states. In fact, problems of such complexity are better treated within the many-particle-Hamiltonian approximation applied in the framework of ab initio wave-function-based theory. In this concept, diagonalization of the above many-particle Hamiltonian (possible also in the presence of external magnetic fields) yields all state energies (ground and excited) of all of the involved multiplets after the action of SOC as well as all of the state contributions. It should be emphasized that diagonalization of the many-particle Hamiltonian automatically yields higher-order terms, which in the sH are commonly modeled by higher powers of the fictitious spin operators. Hence, one can conclude that the sH formalism not only provides a common theoretical framework for different experimental techniques but also offers a convenient interface with theory. Further details regarding our theoretical approach for magnetic systems are given in ref 23. Hence, in an effort to provide a more quantitative picture of the above phenomenon, we employ the many-particle-Hamiltonian approximation and analyze the M_S state compositions of the first five relativistically corrected SA-CASSCF/NEVPT2 $|\Psi_{0-4}\rangle$ states at 0 and 1 T magnetic fields. The obtained data are summarized in Tables 4 and 5. As can be seen, at 0 T, in all of the $|\Psi_{0-4}\rangle$ states, the mixing of the M_S states is very pronounced. As an example, $|\Psi_0\rangle$ is composed of ~65% $|\pm1\rangle$, 20% $|\pm2\rangle$, and 15% $|0\rangle$ spin sublevels, while $|\Psi_1\rangle$ is composed of ~30% $|\pm1\rangle$, ~30% $|\pm2\rangle$, and ~40% $|0\rangle$ spin

https://dx.doi.org/10.1021/acs.inorgchem.0c01636
Inorg. Chem. 2020, 59, 13281−13294

Table 4. Calculated SA-CASSCF/NEVPT2 Energies and M_S State Compositions of the First Five Relativistically Corrected States for Complex $\mathbf{1}_{Mn}$ at 0 and 1 T Magnetic Fields along the *z* Molecular Axis

state	energy (cm^{-1})	$\|+2\rangle$	$\|+1\rangle$	$\|0\rangle$	$\|-1\rangle$	$\|-2\rangle$
0 T Magnetic Field						
$\|\Psi_0\rangle$	0.00	0.10	0.32	0.13	0.32	0.10
$\|\Psi_1\rangle$	0.05	0.14	0.15	0.38	0.15	0.14
$\|\Psi_2\rangle$	11.4	0.13	0.29	0.14	0.29	0.13
$\|\Psi_3\rangle$	11.8	0.34	0.11	0.08	0.11	0.34
$\|\Psi_4\rangle$	15.4	0.26	0.20	0.05	0.20	0.26
1 T Magnetic Field along the *z* Axis						
$\|\Psi_0\rangle$	0.00	0.05	0.05	0.03	0.05	0.81
$\|\Psi_1\rangle$	2.62	0.82	0.02	0.02	0.02	0.05
$\|\Psi_2\rangle$	12.5	0.07	0.01	0.04	0.81	0.07
$\|\Psi_3\rangle$	14.2	0.06	0.80	0.06	0.02	0.06
$\|\Psi_4\rangle$	17.2	0.02	0.08	0.80	0.08	0.02

Table 5. Calculated (4,5) SA-CASSCF/NEVPT2 Magnetic-Dipole-Transition Moments

$$m_{iso,|\Psi_0\rangle\rightarrow|\Psi_{1-4}\rangle}{}^2 = \left|\langle\Psi_0|\sum_i \tfrac{1}{2}[\hat{l}(i) + 2\hat{s}(i)]|\Psi_{1-4}\rangle\right|^2 \text{ in BM}^2$$

Units between $|\Psi_0\rangle \rightarrow |\Psi_{1-4}\rangle$ Relativistically Corrected States (where $m_{iso}{}^2 = m_x{}^2 + m_y{}^2 + m_z{}^2$) for Complex $\mathbf{1}_{Mn}$ at 0 and 1 T Magnetic Fields along the *x*, *y*, and *z* Molecular Axes

transition	energy (cm^{-1})	magnetic dipole (M^2)
0 T Magnetic Field		
$\|\Psi_0\rangle \rightarrow \|\Psi_1\rangle$	0.05	3.55
$\|\Psi_0\rangle \rightarrow \|\Psi_2\rangle$	11.4	1.32
$\|\Psi_0\rangle \rightarrow \|\Psi_3\rangle$	11.7	0.91
$\|\Psi_0\rangle \rightarrow \|\Psi_4\rangle$	15.4	0.007
1 T Magnetic Field along the *x* Axis		
$\|\Psi_0\rangle \rightarrow \|\Psi_1\rangle$	0.3	0.04
$\|\Psi_0\rangle \rightarrow \|\Psi_2\rangle$	11.2	2.32
$\|\Psi_0\rangle \rightarrow \|\Psi_3\rangle$	11.9	0.16
$\|\Psi_0\rangle \rightarrow \|\Psi_4\rangle$	16.5	0.06
1 T Magnetic Field along the *y* Axis		
$\|\Psi_0\rangle \rightarrow \|\Psi_1\rangle$	0.3	0.03
$\|\Psi_0\rangle \rightarrow \|\Psi_2\rangle$	11.1	2.29
$\|\Psi_0\rangle \rightarrow \|\Psi_3\rangle$	11.8	0.20
$\|\Psi_0\rangle \rightarrow \|\Psi_4\rangle$	16.4	0.03
1 T Magnetic Field along the *z* Axis		
$\|\Psi_0\rangle \rightarrow \|\Psi_1\rangle$	2.62	0.02
$\|\Psi_0\rangle \rightarrow \|\Psi_2\rangle$	12.5	2.41
$\|\Psi_0\rangle \rightarrow \|\Psi_3\rangle$	14.2	0.07
$\|\Psi_0\rangle \rightarrow \|\Psi_4\rangle$	17.2	0.03

sublevels. Therefore, these states could be considered to have mainly $|\pm1\rangle$ and $|0\rangle$ M_S character. Consequently, as is also reflected by their slight energy differences, states $|\Psi_0\rangle$ and $|\Psi_1\rangle$ behave as non-Kramers states. In this view, the magnetic-dipole-transition selection rules indicate that the $|\Psi_0\rangle \rightarrow |\Psi_1\rangle$ transition is allowed. In fact, as can be seen in Table 4, this transition contains the largest magnetic-dipole-transition moment. On the other hand, in states $|\Psi_{2-4}\rangle$, the amount of $|0\rangle$ spin sublevel is considerably reduced (Table 4). This effect is associated with a decrease of the respective magnetic-dipole-transition moments of the $|\Psi_0\rangle \rightarrow |\Psi_{2-4}\rangle$ transitions (Table 5). Because of the fact that E/D = 0.0046, one can conclude that, at zero field (0 T), this state mixing (Table 4) arises from the $B_4{}^4$ terms, in agreement with the sH approximation. On the contrary, the energy splitting $|\Psi_{0,1}\rangle$, as well as the composition of states in the presence of 1 T magnetic field, changes radically along the *x*, *y*, and *z* molecular axes. As in the case of the sH analysis, at 1 T the largest energy splitting of $|\Psi_{0,1}\rangle$ states occurs when the magnetic field is aligned along the *z* molecular axis and amounts to 2.49 cm^{-1}. As can be seen in Table 4, the mixing of states is considerably reduced. As a result, the magnetic sublevels $|\Psi_{0,1}\rangle$, $|\Psi_{2,3}\rangle$, and $|\Psi_4\rangle$ contain major contributions from the $|\pm2\rangle$, $|\pm1\rangle$, and $|0\rangle$ M_S states, respectively. This is also reflected in the magnetic-dipole-transition moments of the $|\Psi_0\rangle \rightarrow |\Psi_{2-4}\rangle$ transitions (Table 5). In particular, the $|\Psi_0\rangle \rightarrow |\Psi_1\rangle$ transition is now practically forbidden because it represents a genuine $\Delta M_S = 4$ transition. On the contrary, when the magnetic field is aligned along the *x* and *y* axes, the $|\Psi_0\rangle$ and $|\Psi_1\rangle$ states remain practically degenerate. Hence, the magnetic relaxation cannot be influenced by the external magnetic field along these directions. This is in accordance with the results from the sH analysis, while it is also consistent with the slow magnetic relaxation of complex $\mathbf{1}_{Mn}$ only in the presence of a dc magnetic field, as was observed by ac magnetometry (vide supra). It should be noted that the energy levels of the $|\Psi_0\rangle \rightarrow |\Psi_{1-4}\rangle$ transitions are slightly different from those determined by the sH approach, owing to the small differences between the computed CASSCF/NEVPT2 EPR parameters (Table 2, entry 2) and those determined experimentally by HFEPR.

CONCLUSIONS

In the work presented herein, the magnetic and electronic properties of complex $\mathbf{1}_{Mn}$ were investigated by a host of experimental and computational methods. The magnetic behavior of the magnetically diluted $\mathbf{1}_{Mn}/\mathbf{1}_{Ga}$ system confirmed that the field-induced slow relaxation of magnetization of $\mathbf{1}_{Mn}$[28] stems from the intrinsic properties of its individual molecules. X-band EPR studies of $\mathbf{1}_{Mn}/\mathbf{1}_{Ga}$ made it possible to observe hyperfine interactions between the electronic and nuclear spins in the solid state, a rare observation in Mn(III) complexes. Solution X-band EPR studies of $\mathbf{1}_{Mn}$ revealed the existence of four different S = 2 species, presumably arising from different solution conformations of $\mathbf{1}_{Mn}$, the respective content of which was determined. HFEPR spectroscopy studies provided accurate and precise sH parameters of $\mathbf{1}_{Mn}$, including both the rhombic component E and fourth-order zfs terms, thus resolving the ambiguity of their respective importance for the magnetization relaxation in this system. The findings of our work clearly confirm the necessity of HFEPR studies for this endeavor and were further supported by ab initio wave function quantum-chemical calculations. In particular, a very good agreement between experimentally determined and computed g and hfcc values was achieved, which are consistent with a Mn(III) center in a tetragonally-elongated octahedral coordination environment. It was shown that while the g parameters can be equally well computed at the SA-CASSCF/NEVPT2 and SA-CASSCF/SORCI levels of theory, accurate computations of the hfcc values require that the FC-term contributions are computed at the coupled-cluster level of theory by using unrelaxed response DLPNO−CCSD spin densities. The accurate determination of the zfs components of $\mathbf{1}_{Mn}$ revealed a very small rhombicity (E/D = 0.0046). Computational studies, at both the SA-CASSCF/NEVPT2 and SA-CASSCF/SORCI levels of theory, confirmed these findings and quantified the contribution of SSC and SOC to the magnitude of D. Moreover, the latter studies provided

https://dx.doi.org/10.1021/acs.inorgchem.0c01636
Inorg. Chem. 2020, 59, 13281−13294

evidence of a pronounced mixing between the $|\pm2\rangle$, $|\pm1\rangle$, and $|0\rangle$ magnetic sublevels of the $S = 2$ complex $\mathbf{1}_{Mn}$, in the absence of a dc magnetic field. This mixing of states relaxes the ($\Delta M_S = 4$) selection rule of the nominally forbidden magnetic-dipole transition between the lowest-energy $|+2\rangle$ and $|-2\rangle$ magnetic sublevels. Hence, this effect, which is mainly attributed to the fourth-order zfs terms rather than the rhombic zfs component E, is responsible for the observed fast magnetic relaxation of $\mathbf{1}_{Mn}$ in the absence of an external dc field.[28] On the contrary, in the presence of an external magnetic field (>0.1 T), the mixing of states is strongly reduced and the ($\Delta M_S = 4$) selection rule becomes effective, thus precluding the magnetic-dipole transition between the lowest-energy $|+2\rangle$ and $|-2\rangle$ magnetic sublevels. The above findings justify the experimental fact that complex $\mathbf{1}_{Mn}$ exhibits slow relaxation of its magnetization only in the presence of an external dc magnetic field.

■ ASSOCIATED CONTENT

Supporting Information

The Supporting Information is available free of charge at https://pubs.acs.org/doi/10.1021/acs.inorgchem.0c01636.

Elemental analyses of Mn and Ga (Tables S1 and S2), ac magnetometry (Figures S1−S14 and Table S3), micro-SQUID (Figure S15) data for $\mathbf{1}_{Mn}/\mathbf{1}_{Ga}$, parallel-mode X-band EPR data for $\mathbf{1}_{Mn}$ (Table S4), experimental details of HFEPR and data for $\mathbf{1}_{Mn}$ (Figures S16−S18), perpendicular-mode X-band spectra of $\mathbf{1}_{Mn}$ and $\mathbf{1}_{Mn}/\mathbf{1}_{Ga}$ (Figure S19), parallel-mode X-band EPR data of $\mathbf{1}_{Mn}$ (Figure S20), dependence on the zfs parameters of the dual-mode X-band EPR signals originating from the $|\pm2\rangle$ doublet of an $S = 2$ system (related analysis and Figure S21), and magnetic sublevel analysis and transition probabilities based on the sH formalism (Tables S5−S12) (PDF)

■ AUTHOR INFORMATION

Corresponding Authors

Yiannis Sanakis − *Institute of Nanoscience and Nanotechnolgy, National Centre of Scientific Research "Demokritos", Aghia Paraskevi 15310, Attiki, Greece*; Email: i.sanakis@inn.demokritos.gr

J. Krzystek − *National High Magnetic Field Laboratory, Florida State University, Tallahassee, Florida 32310, United States;* orcid.org/0000-0001-6088-1936; Email: krzystek@magnet.fsu.edu

Panayotis Kyritsis − *Inorganic Chemistry Laboratory, Department of Chemistry, National and Kapodistrian University of Athens, 15771 Athens, Greece;* orcid.org/0000-0002-3908-4649; Email: kyritsis@chem.uoa.gr

Authors

Dimitrios Maganas − *Max-Planck-Institut für Kohlenforschung, 45470 Mülheim an der Ruhr, Germany*

Alexios Grigoropoulos − *Inorganic Chemistry Laboratory, Department of Chemistry, National and Kapodistrian University of Athens, 15771 Athens, Greece*

Eleftherios Ferentinos − *Inorganic Chemistry Laboratory, Department of Chemistry, National and Kapodistrian University of Athens, 15771 Athens, Greece*

Marios G. Kostakis − *Analytical Chemistry Laboratory, Department of Chemistry, National and Kapodistrian University of Athens, 15771 Athens, Greece*

Vasiliki Petroulea − *Institute of Nanoscience and Nanotechnolgy, National Centre of Scientific Research "Demokritos", Aghia Paraskevi 15310, Attiki, Greece*

Michael Pissas − *Institute of Nanoscience and Nanotechnolgy, National Centre of Scientific Research "Demokritos", Aghia Paraskevi 15310, Attiki, Greece*

Komalavalli Thirunavukkuarasu − *Department of Physics, Florida A&M University, Tallahassee, Florida 32307, United States;* orcid.org/0000-0001-6148-2670

Wolfgang Wernsdorfer − *Physikalisches Institut and Institute of Quantum Materials and Technologies, Karlsruher Institut für Technologie, 76131 Karlsruhe, Germany;* orcid.org/0000-0003-4602-5257

Frank Neese − *Max-Planck-Institut für Kohlenforschung, 45470 Mülheim an der Ruhr, Germany;* orcid.org/0000-0003-4691-0547

Complete contact information is available at: https://pubs.acs.org/10.1021/acs.inorgchem.0c01636

Notes

The authors declare no competing financial interest.

■ ACKNOWLEDGMENTS

This work was supported by the Special Research Account of the National and Kapodistrian University of Athens (NKUA; P.K.) and the Max Planck Society (D.M. and F.N.). Part of this work was performed at the National High Magnetic Field Laboratory (NHMFL), funded by the National Science Foundation through Cooperative Agreements DMR 1157490 and 1644779 and the State of Florida. E.F. has been awarded a State Scholarship Foundation (IKY) fellowship, by the act "Support for Postdoctoral Researchers", from the operational program "Human Power Development, Education and Lifelong Learning" (6, 8, and 9 priority axes), cofunded by the European Social Fund and the Greek State. M.P. and Y.S. acknowledge support by Project MIS 5002567, implemented under the "Action for the Strategic Development on the Research and Technological Sector", funded by the Operational Programme "Competitiveness, Entrepreneurship and Innovation" (NSRF 2014−2020), and cofinanced by Greece and the European Union (European Regional Development Fund). P.K. thanks the Fulbright Foundation in Greece and the NHMFL Visiting Scientist program for supporting his visit to the NHMFL, during which the HFEPR results were obtained. Dr. A. Ozarowski is acknowledged for his EPR fit and simulation program *SPIN*, Prof. M. Hendrich for his EPR fit and simulation program *SpinCount* and Prof. N. Thomaidis (Analytical Chemistry Laboratory, NKUA) for providing the facilities for Mn/Ga elemental analysis. We also thank the reviewers of the manuscript for their very constructive comments.

■ REFERENCES

(1) Sessoli, R.; Gatteschi, D.; Caneschi, A.; Novak, M. A. Magnetic Bistability in a Metal-Ion Cluster. *Nature* **1993**, *365*, 141−143.

(2) Gatteschi, D.; Bogani, L.; Cornia, A.; Mannini, M.; Sorace, L.; Sessoli, R. Molecular magnetism, status and perspectives. *Solid State Sci.* **2008**, *10*, 1701−1709.

(3) Stamp, P. C. E.; Gaita-Arino, A. Spin-based quantum computers made by chemistry: hows and whys. *J. Mater. Chem.* **2009**, *19*, 1718−1730.

(4) Ferrando-Soria, J.; Vallejo, J.; Castellano, M.; Martinez-Lillo, J.; Pardo, E.; Cano, J.; Castro, I.; Lloret, F.; Ruiz-Garcia, R.; Julve, M.

Molecular magnetism, quo vadis? A historical perspective from a coordination chemist viewpoint. *Coord. Chem. Rev.* **2017**, *339*, 17−103.
(5) Sharples, J. W.; Collison, D. Coordination compounds and the magnetocaloric effect. *Polyhedron* **2013**, *54*, 91−103.
(6) Milios, C. J.; Vinslava, A.; Wernsdorfer, W.; Moggach, S.; Parsons, S.; Perlepes, S. P.; Christou, G.; Brechin, E. K. A record anisotropy barrier for a single-molecule magnet. *J. Am. Chem. Soc.* **2007**, *129*, 2754−2755.
(7) Cirera, J.; Ruiz, E.; Alvarez, S.; Neese, F.; Kortus, J. How to Build Molecules with Large Magnetic Anisotropy. *Chem. - Eur. J.* **2009**, *15*, 4078−4087.
(8) Bagai, R.; Christou, G. The *Drosophila* of single-molecule magnetism: $Mn_{12}O_{12}(O_2CR)_{16}(H_2O)_4$. *Chem. Soc. Rev.* **2009**, *38*, 1011−1026.
(9) Milios, C. J.; Winpenny, R. E. P. Cluster-Based Single-Molecule Magnets. In *Molecular Nanomagnets and Related Phenomena*; Gao, S., Ed.; Structure and Bonding; Springer: Berlin, 2015; Vol. *164*; pp 1−109.
(10) Ruiz, E.; Cirera, J.; Cano, J.; Alvarez, S.; Loose, C.; Kortus, J. Can large magnetic anisotropy and high spin really coexist? *Chem. Commun.* **2008**, 52−54.
(11) Neese, F.; Pantazis, D. A. What is not required to make a single molecule magnet. *Faraday Discuss.* **2011**, *148*, 229−238.
(12) Waldmann, O. A Criterion for the Anisotropy Barrier in Single-Molecule Magnets. *Inorg. Chem.* **2007**, *46*, 10035−10037.
(13) Aldoshin, S. M.; Korchagin, D. V.; Palii, A. V.; Tsukerblat, B. S. Some new trends in the design of single molecule magnets. *Pure Appl. Chem.* **2017**, *89*, 1119−1143.
(14) Goodwin, C. A. P.; Ortu, F.; Reta, D. Strangely attractive: Collaboration and feedback in the field of molecular magnetism. *Int. J. Quantum Chem.* **2020**, *120*, e26248.
(15) Goodwin, C. A. P.; Ortu, F.; Reta, D.; Chilton, N. F.; Mills, D. P. Molecular magnetic hysteresis at 60 K in dysprosocenium. *Nature* **2017**, *548*, 439−442.
(16) Guo, F. S.; Day, B. M.; Chen, Y. C.; Tong, M. L.; Mansikkamaki, A.; Layfield, R. A. A Dysprosium Metallocene Single-Molecule Magnet Functioning at the Axial Limit. *Angew. Chem., Int. Ed.* **2017**, *56*, 11445−11449.
(17) Randall McClain, K.; Gould, C. A.; Chakarawet, K.; Teat, S. J.; Groshens, T. J.; Long, J. R.; Harvey, B. G. High-temperature magnetic blocking and magneto-structural correlations in a series of dysprosium(III) metallocenium single-molecule magnets. *Chem. Sci.* **2018**, *9*, 8492−8503.
(18) Guo, F. S.; Day, B. M.; Chen, Y. C.; Tong, M. L.; Mansikkamaki, A.; Layfield, R. A. Magnetic hysteresis up to 80 K in a dysprosium metallocene single-molecule magnet. *Science* **2018**, *362*, 1400−1403.
(19) Craig, G. A.; Murrie, M. 3d single-ion magnets. *Chem. Soc. Rev.* **2015**, *44*, 2135−2147.
(20) Bar, A. K.; Pichon, C.; Sutter, J. P. Magnetic anisotropy in two- to eight-coordinated transition-metal complexes: Recent developments in molecular magnetism. *Coord. Chem. Rev.* **2016**, *308*, 346−380.
(21) Frost, J. M.; Harriman, K. L. M.; Murugesu, M. The rise of 3-d single-ion magnets in molecular magnetism: towards materials from molecules? *Chem. Sci.* **2016**, *7*, 2470−2491.
(22) Feng, M.; Tong, M.-L. Single Ion Magnets from 3d to 5f: Developments and Strategies. *Chem. - Eur. J.* **2018**, *24*, 7574−7594.
(23) Atanasov, M.; Aravena, D.; Suturina, E.; Bill, E.; Maganas, D.; Neese, F. First principles approach to the electronic structure, magnetic anisotropy and spin relaxation in mononuclear 3d-transition metal single molecule magnets. *Coord. Chem. Rev.* **2015**, *289*, 177−214.
(24) Gomez-Coca, S.; Aravena, D.; Morales, R.; Ruiz, E. Large magnetic anisotropy in mononuclear metal complexes. *Coord. Chem. Rev.* **2015**, *289*, 379−392.
(25) Goswami, S.; Mondal, A. K.; Konar, S. Nanoscopic molecular magnets. *Inorg. Chem. Front.* **2015**, *2*, 687−712.
(26) Ishikawa, R.; Miyamoto, R.; Nojiri, H.; Breedlove, B. K.; Yamashita, M. Slow Relaxation of the Magnetization of an Mn^{III} Single Ion. *Inorg. Chem.* **2013**, *52*, 8300−8302.
(27) Vallejo, J.; Pascual-Alvarez, A.; Cano, J.; Castro, I.; Julve, M.; Lloret, F.; Krzystek, J.; De Munno, G.; Armentano, D.; Wernsdorfer, W.; Ruiz-Garcia, R.; Pardo, E. Field-Induced Hysteresis and Quantum Tunneling of the Magnetization in a Mononuclear Manganese(III) Complex. *Angew. Chem., Int. Ed.* **2013**, *52*, 14075−14079.
(28) Grigoropoulos, A.; Pissas, M.; Papatolis, P.; Psycharis, V.; Kyritsis, P.; Sanakis, Y. Spin-Relaxation Properties of a High-Spin Mononuclear $Mn^{III}O_6$-Containing Complex. *Inorg. Chem.* **2013**, *52*, 12869−12871.
(29) Craig, G. A.; Marbey, J. J.; Hill, S.; Roubeau, O.; Parsons, S.; Murrie, M. Field-Induced Slow Relaxation in a Monometallic Manganese(III) Single-Molecule Magnet. *Inorg. Chem.* **2015**, *54*, 13−15.
(30) Chen, L.; Wang, J.; Liu, Y.-Z.; Song, Y.; Chen, X.-T.; Zhang, Y.-Q.; Xue, Z.-L. Slow Magnetic Relaxation in Mononuclear Octahedral Manganese(III) Complexes with Dibenzoylmethanide Ligands. *Eur. J. Inorg. Chem.* **2015**, *2015*, 271−278.
(31) Sato, R.; Suzuki, K.; Minato, T.; Shinoe, M.; Yamaguchi, K.; Mizuno, N. Field-induced slow magnetic relaxation of octahedrally coordinated mononuclear Fe(III)-, Co(II)-, and Mn(III)-containing polyoxometalates. *Chem. Commun.* **2015**, *51*, 4081−4084.
(32) Abherve, A.; Palacios-Corella, M.; Clemente-Juan, J. M.; Marx, R.; Neugebauer, P.; van Slageren, J.; Clemente-Leon, M.; Coronado, E. Bimetallic Mn^{III}-Fe^{II} hybrid complexes formed by a functionalized Mn^{III} Anderson polyoxometalate coordinated to Fe^{II}: observation of a field-induced slow relaxation of magnetization in the Mn^{III} centres and a photoinduced spin-crossover in the Fe-II centres. *J. Mater. Chem. C* **2015**, *3*, 7936−7945.
(33) Realista, S.; Fitzpatrick, A. J.; Santos, G.; Ferreira, L. P.; Barroso, S.; Pereira, L. C. J.; Bandeira, N. A. G.; Neugebauer, P.; Hruby, J.; Morgan, G. G.; van Slageren, J.; Calhorda, M. J.; Martinho, P. N. A Mn(III) single ion magnet with tridentate Schiff-base ligands. *Dalton Trans.* **2016**, *45*, 12301−12307.
(34) Liu, Y. M.; Liu, Z. Y.; Yang, E. C.; Zhao, X. J. Field-induced slow relaxation of a manganese(III)-based single-ion magnet. *Inorg. Chem. Commun.* **2017**, *77*, 27−30.
(35) Escobar, L. B. L.; Guedes, G. P.; Soriano, S.; Cassaro, R. A. A.; Marbey, J.; Hill, S.; Novak, M. A.; Andruh, M.; Vaz, M. G. F. Synthesis, Crystal Structures, and EPR Studies of First $Mn^{III}Ln^{III}$ Hetero-binuclear Complexes. *Inorg. Chem.* **2018**, *57*, 326−334.
(36) Pascual-Alvarez, A.; Vallejo, J.; Pardo, E.; Julve, M.; Lloret, F.; Krzystek, J.; Armentano, D.; Wernsdorfer, W.; Cano, J. Field-Induced Slow Magnetic Relaxation in a Mononuclear Manganese(III)-Porphyrin Complex. *Chem. - Eur. J.* **2015**, *21*, 17299−17307.
(37) Nemec, I.; Herchel, R.; Travnicek, Z.; Silha, T. Field-induced slow relaxation of magnetization in dinuclear and trinuclear Co^{III}···Mn^{III} complexes. *RSC Adv.* **2016**, *6*, 3074−3083.
(38) Dolai, M.; Mondal, A.; Liu, J. L.; Ali, M. Three novel mononuclear Mn(III)-based magnetic materials with square pyramidal versus octahedral geometries. *New J. Chem.* **2017**, *41*, 10890−10898.
(39) Mon, M.; Pascual-Alvarez, A.; Grancha, T.; Cano, J.; Ferrando-Soria, J.; Lloret, F.; Gascon, J.; Pasan, J.; Armentano, D.; Pardo, E. Solid-State Molecular Nanomagnet Inclusion into a Magnetic Metal-Organic Framework: Interplay of the Magnetic Properties. *Chem. - Eur. J.* **2016**, *22*, 539−545.
(40) Fetoh, A.; Cosquer, G.; Morimoto, M.; Irie, M.; El-Gammal, O.; Abu El-Reash, G. M.; Breedlove, B. K.; Yamashita, M. Synthesis, Structures, and Magnetic Properties of Two Coordination Assemblies of Mn(III) Single Molecule Magnets Bridged via Photochromic Diarylethene Ligands. *Inorg. Chem.* **2019**, *58*, 2307−2314.
(41) Zuniga-Villareal, N.; Lezama, M. R.; Hernandez-Ortega, S.; Silvestru, C. Crystal and molecular structure of $Mn[(OPPh_2)_2N]_3 \cdot CH_2Cl_2$, a new monomeric manganese(III) complex stabilized by oxygen chelating ligands. *Polyhedron* **1998**, *17*, 2679−2685.

https://dx.doi.org/10.1021/acs.inorgchem.0c01636
Inorg. Chem. 2020, 59, 13281−13294

(42) Dexheimer, S. L.; Gohdes, J. W.; Chan, M. K.; Hagen, K. S.; Armstrong, W. H.; Klein, M. P. Detection of EPR spectra in $S = 2$ states of trivalent manganese complexes. *J. Am. Chem. Soc.* **1989**, *111*, 8923−8925.
(43) Bryliakov, K. P.; Babushkin, D. E.; Talsi, E. P. Detection of EPR spectra in $S = 2$ states of Mn^{III}(salen) complexes. *Mendeleev Commun.* **1999**, *9*, 29−32.
(44) Campbell, K. A.; Yikilmaz, E.; Grant, C. V.; Gregor, W.; Miller, A.-F.; Britt, R. D. Parallel Polarization EPR Characterization of the Mn(III) Center of Oxidized Manganese Superoxide Dismutase. *J. Am. Chem. Soc.* **1999**, *121*, 4714−4715.
(45) Bryliakov, K. P.; Khavrutskii, I. V.; Talsi, E. P.; Kholdeeva, O. A. EPR detection and characterization of high-valent manganese complexes in Mn^{III}(Salen) catalyzed aerobic olefin epoxidation. *React. Kinet. Catal. Lett.* **2000**, *71*, 183−191.
(46) Campbell, K. A.; Lashley, M. R.; Wyatt, J. K.; Nantz, M. H.; Britt, R. D. Dual-Mode EPR Study of Mn(III) Salen and the Mn(III) Salen-Catalyzed Epoxidation of *cis-β*-Methylstyrene. *J. Am. Chem. Soc.* **2001**, *123*, 5710−5719.
(47) Talsi, E. P.; Bryliakov, K. P. X-band perpendicular-mode EPR spectra of ″EPR-silent″ manganese(III) porphyrins. *Mendeleev Commun.* **2004**, *14*, 111−112.
(48) Cazacu, M.; Shova, S.; Soroceanu, A.; Machata, P.; Bucinsky, L.; Breza, M.; Rapta, P.; Telser, J.; Krzystek, J.; Arion, V. B. Charge and Spin States in Schiff Base Metal Complexes with a Disiloxane Unit Exhibiting a Strong Noninnocent Ligand Character: Synthesis, Structure, Spectroelectrochemistry, and Theoretical Calculations. *Inorg. Chem.* **2015**, *54*, 5691−5706.
(49) Abragam, A.; Bleaney, B.: *Electron Paramagnetic Resonance of Transition Ions*; Dover Publications: New York, 1986.
(50) Krzystek, J.; Ozarowski, A.; Telser, J. Multi-frequency, high-field EPR as a powerful tool to accurately determine zero-field splitting in high-spin transition metal coordination complexes. *Coord. Chem. Rev.* **2006**, *250*, 2308−2324.
(51) Telser, J.; Ozarowski, A.; Krzystek, J. High-frequency and -field electron paramagnetic resonance of transition metal ion (d block) coordination complexes. *Electron Paramagn. Reson.* **2012**, *23*, 209−263.
(52) Krzystek, J.; Telser, J. Measuring giant anisotropy in paramagnetic transition metal complexes with relevance to single-ion magnetism. *Dalton Trans.* **2016**, *45*, 16751−16763.
(53) Barra, A.-L.; Gatteschi, D.; Sessoli, R.; Abbati, G. L.; Cornia, A.; Fabretti, A. C.; Uytterhoeven, M. G. Electronic structure of manganese(III) compounds from high-frequency EPR spectra. *Angew. Chem., Int. Ed. Engl.* **1997**, *36*, 2329−2331.
(54) Goldberg, D. P.; Telser, J.; Krzystek, J.; Montalban, A. G.; Brunel, L.-C.; Barrett, A. G. M.; Hoffman, B. M. EPR Spectra from ″EPR-Silent″ Species: High-Field EPR Spectroscopy of Manganese(III) Porphyrins. *J. Am. Chem. Soc.* **1997**, *119*, 8722−8723.
(55) Krzystek, J.; Telser, J.; Pardi, L. A.; Goldberg, D. P.; Hoffman, B. M.; Brunel, L.-C. High-frequency and -field electron paramagnetic resonance of high-spin manganese(III) in porphyrinic complexes. *Inorg. Chem.* **1999**, *38*, 6121−6129.
(56) Limburg, J.; Vrettos, J. S.; Crabtree, R. H.; Brudvig, G. W.; de Paula, J. C.; Hassan, A.; Barra, A.-L.; Duboc-Toia, C.; Collomb, M.-N. High-Frequency EPR Study of a New Mononuclear Manganese(III) Complex: [(terpy)$Mn(N_3)_3$] (terpy = 2,2′:6′,2″-Terpyridine). *Inorg. Chem.* **2001**, *40*, 1698−1703.
(57) Mossin, S.; Stefan, M.; ter Heerdt, P.; Bouwen, A.; Goovaerts, E.; Weihe, H. Fourth-order zero-field splitting parameters of [Mn(cyclam)Br_2]Br determined by single-crystal W-band EPR. *Appl. Magn. Reson.* **2001**, *21*, 587−596.
(58) Krzystek, J.; Pardi, L. A.; Brunel, L.-C.; Goldberg, D. P.; Hoffman, B. M.; Licoccia, S.; Telser, J. High-frequency and -field electron paramagnetic resonance of high-spin manganese(III) in tetrapyrrole complexes. *Spectrochim. Acta, Part A* **2002**, *58A*, 1113−1127.
(59) Krzystek, J.; Yeagle, G. J.; Park, J.-H.; Britt, R. D.; Meisel, M. W.; Brunel, L.-C.; Telser, J. High-Frequency and -Field EPR Spectroscopy of Tris(2,4-pentanedionato)manganese(III): Investigation of Solid-State versus Solution Jahn-Teller Effects. *Inorg. Chem.* **2003**, *42*, 4610−4618.
(60) Mantel, C.; Hassan, A. K.; Pecaut, J.; Deronzier, A.; Collomb, M.-N.; Duboc-Toia, C. A High-Frequency and High-Field EPR Study of New Azide and Fluoride Mononuclear Mn(III) Complexes. *J. Am. Chem. Soc.* **2003**, *125*, 12337−12344.
(61) Tregenna-Piggott, P. L. W.; Weihe, H.; Barra, A.-L. High-Field, Multifrequency EPR Study of the $[Mn(OH_2)_6]^{3+}$ Cation: Influence of *π*-Bonding on the Ground State Zero-Field-Splitting Parameters. *Inorg. Chem.* **2003**, *42*, 8504−8508.
(62) Albela, B.; Carina, R.; Policar, C.; Poussereau, S.; Cano, J.; Guilhem, J.; Tchertanov, L.; Blondin, G.; Delroisse, M.; Girerd, J.-J. Synthesis and X-ray Structure of the $Mn^{II}Cl_2$ and $Mn^{III}F_2$ Complexes of N,N′-Dimethyl-2,11-diaza[3,3](2,6)pyridinophane. High-Field Electron Paramagnetic Resonance and Density Functional Theory Studies of the Mn(III) Complex. Evidence for a Low-Lying Spin Triplet State. *Inorg. Chem.* **2005**, *44*, 6959−6966.
(63) Aromi, G.; Telser, J.; Ozarowski, A.; Brunel, L.-C.; Stoeckli-Evans, H.-M.; Krzystek, J. Synthesis, Crystal Structure, and High-Precision High-Frequency and -Field Electron Paramagnetic Resonance Investigation of a Manganese(III) Complex: [Mn(dbm)$_2$(py)$_2$](ClO_4). *Inorg. Chem.* **2005**, *44*, 187−196.
(64) Harvey, J. D.; Ziegler, C. J.; Telser, J.; Ozarowski, A.; Krzystek, J. High-Frequency and -Field EPR Investigation of a Manganese(III) N-Confused Porphyrin Complex, [Mn(NCTPP)(py)$_2$]. *Inorg. Chem.* **2005**, *44*, 4451−4453.
(65) Krivokapic, I.; Noble, C.; Klitgaard, S.; Tregenna-Piggott, P.; Weihe, H.; Barra, A.-L. Anisotropic hyperfine interaction in the manganese(III) hexaaqua ion. *Angew. Chem., Int. Ed.* **2005**, *44*, 3613−3616.
(66) Mantel, C.; Chen, H.; Crabtree, R. H.; Brudvig, G. W.; Pecaut, J.; Collomb, M.-N.; Duboc, C. High-spin chloro mononuclear Mn^{III} complexes: a multifrequency high-field EPR study. *ChemPhysChem* **2005**, *6*, 541−546.
(67) Horitani, M.; Yashiro, H.; Hagiwara, M.; Hori, H. Multi-frequency and high-field EPR study of manganese(III) protoporphyrin IX reconstituted myoglobin with an $S = 2$ integer electron spin. *J. Inorg. Biochem.* **2008**, *102*, 781−788.
(68) Scheifele, Q.; Riplinger, C.; Neese, F.; Weihe, H.; Barra, A.-L.; Juranyi, F.; Podlesnyak, A.; Tregenna-Piggott, P. L. W. Spectroscopic and Theoretical Study of a Mononuclear Manganese(III) Complex Exhibiting a Tetragonally Compressed Geometry. *Inorg. Chem.* **2008**, *47*, 439−447.
(69) Romain, S.; Duboc, C.; Neese, F.; Riviere, E.; Hanton, L. R.; Blackman, A. G.; Philouze, C.; Lepretre, J.-C.; Deronzier, A.; Collomb, M.-N. An unusual stable mononuclear Mn^{III} bis-terpyridine complex exhibiting Jahn-Teller compression: electrochemical synthesis, physical characterisation and theoretical study. *Chem. - Eur. J.* **2009**, *15*, 980−988.
(70) Mossin, S.; Weihe, H.; Barra, A. L. Is the axial zero-field splitting parameter of tetragonally elongated high-spin manganese(III) complexes always negative? *J. Am. Chem. Soc.* **2002**, *124*, 8764−8765.
(71) Duboc, C. Determination and prediction of the magnetic anisotropy of Mn ions. *Chem. Soc. Rev.* **2016**, *45*, 5834−5847.
(72) Houton, E.; Kelly, B.; Sanz, S.; McInnes, E. J. L.; Collison, D.; Brechin, E. K.; Barra, A. L.; Ryder, A. G.; Jones, L. F. A Facile Synthetic Route to a Family of Mn-III Monomers and Their Structural, Magnetic and Spectroscopic Studies. *Eur. J. Inorg. Chem.* **2016**, *2016*, 5123−5131.
(73) Krzystek, J.; Telser, J.; Li, J.; Subramanian, M. A. Magnetic Properties and Electronic Structure of Manganese-Based Blue Pigments: A High-Frequency and -Field EPR Study. *Inorg. Chem.* **2015**, *54*, 9040−9045.
(74) Gatteschi, D.; Sessoli, R. Quantum tunneling of magnetization and related phenomena in molecular materials. *Angew. Chem., Int. Ed.* **2003**, *42*, 268−297.

https://dx.doi.org/10.1021/acs.inorgchem.0c01636
Inorg. Chem. 2020, 59, 13281−13294

(75) del Barco, E.; Kent, A. D.; Hill, S.; North, J. M.; Dalal, N. S.; Rumberger, E. M.; Hendrickson, D. N.; Chakov, N.; Christou, G. Magnetic quantum tunneling in the single-molecule magnet Mn_{12}-acetate. *J. Low Temp. Phys.* **2005**, *140*, 119−174.
(76) GarciaMontalvo, V.; CeaOlivares, R.; Williams, D. J.; EspinosaPerez, G. Stereochemical consequences of the bismuth atom electron lone pair, a comparison between MX_6E and MX_6 systems. Crystal and molecular structures of tris[N-(P,P-diphenylphosphinonoyl)-P,P-diphenylphosphinimidato]bismuth(III), $[Bi\{(OPPh_2)_2N\}_3]$, -indium(III), $[In\{(OPPh_2)_2N\}_3]\cdot C_6H_6$, and -gallium(III), $[Ga\{(OPPh_2)_2N\}_3]\cdot CH_2Cl_2$. *Inorg. Chem.* **1996**, *35*, 3948−3953.
(77) Boca, R. Zero-field splitting in metal complexes. *Coord. Chem. Rev.* **2004**, *248*, 757−815.
(78) Neese, F. Quantum Chemistry and EPR Parameters. *eMagRes.* **2017**, *6*, 1−22.
(79) Wernsdorfer, W. Classical and quantum magnetization reversal studied in nanometer-sized particles and clusters. *Adv. Chem. Phys.* **2007**, *118*, 99−190.
(80) Wernsdorfer, W. From micro- to nano-SQUIDs: applications to nanomagnetism. Supercond. *Supercond. Sci. Technol.* **2009**, *22*, No. 064013.
(81) Hassan, A. K.; Pardi, L. A.; Krzystek, J.; Sienkiewicz, A.; Goy, P.; Rohrer, M.; Brunel, L. C. Ultrawide Band Multifrequency High-Field EMR Technique: A Methodology for Increasing Spectroscopic Information. *J. Magn. Reson.* **2000**, *142*, 300−312.
(82) Neese, F. The ORCA program system. *Wiley Interdiscip. Rev.: Comput. Mol. Sci.* **2012**, *2*, 73−78.
(83) Becke, A. D. Density-Functional Exchange-Energy Approximation with Correct Asymptotic-Behavior. *Phys. Rev. A: At., Mol., Opt. Phys.* **1988**, *38*, 3098−3100.
(84) Perdew, J. P. Density-Functional Approximation for the Correlation-Energy of the Inhomogeneous Electron-Gas. *Phys. Rev. B: Condens. Matter Mater. Phys.* **1986**, *33*, 8822−8824.
(85) Schäfer, A.; Huber, C.; Ahlrichs, R. Fully optimized contracted Gaussian basis sets of triple zeta valence quality for atoms Li to Kr. *J. Chem. Phys.* **1994**, *100*, 5829−5835.
(86) Weigend, F.; Ahlrichs, R. Balanced basis sets of split valence, triple zeta valence and quadruple zeta valence quality for H to Rn: Design and assessment of accuracy. *Phys. Chem. Chem. Phys.* **2005**, *7*, 3297−3305.
(87) Schäfer, A.; Horn, H.; Ahlrichs, R. Fully optimized contracted Gaussian basis sets for atoms Li to Kr. *J. Chem. Phys.* **1992**, *97*, 2571−2577.
(88) Grimme, S.; Antony, J.; Ehrlich, S.; Krieg, H. A consistent and accurate ab initio parametrization of density functional dispersion correction (DFT-D) for the 94 elements H-Pu. *J. Chem. Phys.* **2010**, *132*, No. 154104.
(89) Grimme, S.; Ehrlich, S.; Goerigk, L. Effect of the Damping Function in Dispersion Corrected Density Functional Theory. *J. Comput. Chem.* **2011**, *32*, 1456−1465.
(90) Neese, F. An improvement of the resolution of the identity approximation for the formation of the Coulomb matrix. *J. Comput. Chem.* **2003**, *24*, 1740−1747.
(91) Roos, B. O.; Taylor, P. R.; Sigbahn, P. E. M. A Complete Active Space SCF Method (CACCF) Using a Density-Matrix Formulated Super-CI Approach. *Chem. Phys.* **1980**, *48*, 157−173.
(92) Siegbahn, P. E. M.; Almlof, J.; Heiberg, A.; Roos, B. O. The Complete Active Space SCF (CACCF) Method in a Newton-Raphson Formulation with Application to the HNO Molecule. *J. Chem. Phys.* **1981**, *74*, 2384−2396.
(93) Angeli, C.; Cimiraglia, R.; Evangelisti, S.; Leininger, T.; Malrieu, J.-P. Introduction of n-electron valence states for multireference perturbation theory. *J. Chem. Phys.* **2001**, *114*, 10252−10264.
(94) Angeli, C.; Cimiraglia, R. Multireference perturbation configuration interaction V. Third-order energy contributions in the Møller−Plesset and Epstein−Nesbet partitions. *Theor. Chem. Acc.* **2002**, *107*, 313−317.
(95) Neese, F. A spectroscopy oriented configuration interaction procedure. *J. Chem. Phys.* **2003**, *119*, 9428−9443.
(96) Pantazis, D. A.; Chen, X. Y.; Landis, C. R.; Neese, F. All-electron scalar relativistic basis sets for third-row transition metal atoms. *J. Chem. Theory Comput.* **2008**, *4*, 908−919.
(97) Hess, B. A. Relativistic Electronic-Structure Calculations Employing a 2-Component No-Pair Formalism with External-Field Projection Operators. *Phys. Rev. A: At., Mol., Opt. Phys.* **1986**, *33*, 3742−3748.
(98) Neese, F. Efficient and accurate approximations to the molecular spin-orbit coupling operator and their use in molecular g-tensor calculations. *J. Chem. Phys.* **2005**, *122*, 034107.
(99) Ganyushin, D.; Neese, F. A fully variational spin-orbit coupled complete active space self-consistent field approach: application to electron paramagnetic resonance g-tensors. *J. Chem. Phys.* **2013**, *138*, 104113.
(100) Vallet, V.; Maron, L.; Teichteil, C.; Flament, J.-P. A two-step uncontracted determinantal effective Hamiltonian-based SO−CI method. *J. Chem. Phys.* **2000**, *113*, 1391−1402.
(101) Maurice, R.; Bastardis, R.; Graaf, C. d.; Suaud, N.; Mallah, T.; Guihéry, N. Universal Theoretical Approach to Extract Anisotropic Spin Hamiltonians. *J. Chem. Theory Comput.* **2009**, *5*, 2977−2984.
(102) Neese, F. Sum-over-states based multireference ab initio calculation of EPR spin Hamiltonian parameters for transition metal complexes. A case study. *Magn. Reson. Chem.* **2004**, *42*, S187−S198.
(103) Neese, F. Correlated ab initio calculation of electronic *g*-tensors using a sum over states formulation. *Chem. Phys. Lett.* **2003**, *380*, 721−728.
(104) Neese, F. Analytic derivative calculation of electronic *g*-tensors based on multireference configuration interaction wave functions. *Mol. Phys.* **2007**, *105*, 2507−2514.
(105) Saitow, M.; Becker, U.; Riplinger, C.; Valeev, E. F.; Neese, F. A new near-linear scaling, efficient and accurate, open-shell domain-based local pair natural orbital coupled cluster singles and doubles theory. *J. Chem. Phys.* **2017**, *146*, 164105.
(106) Saitow, M.; Neese, F. Accurate spin-densities based on the domain-based local pair-natural orbital coupled-cluster theory. *J. Chem. Phys.* **2018**, *149*, 034104.
(107) Maganas, D.; Grigoropoulos, A.; Staniland, S. S.; Chatziefthimiou, S. D.; Harrison, A.; Robertson, N.; Kyritsis, P.; Neese, F. Tetrahedral and Square Planar $Ni[(SPR_2)_2N]_2$ complexes, R = Ph &^{i}Pr Revisited: Experimental and Theoretical Analysis of Interconversion Pathways, Structural Preferences, and Spin Delocalization. *Inorg. Chem.* **2010**, *49*, 5079−5093.
(108) Zadrozny, J. M.; Long, J. R. Slow Magnetic Relaxation at Zero Field in the Tetrahedral Complex $[Co(SPh)_4]^{2-}$. *J. Am. Chem. Soc.* **2011**, *133*, 20732−20734.
(109) Sottini, S.; Poneti, G.; Ciattini, S.; Levesanos, N.; Ferentinos, E.; Krzystek, J.; Sorace, L.; Kyritsis, P. Magnetic Anisotropy of Tetrahedral Co^{II} Single-Ion Magnets: Solid-State Effects. *Inorg. Chem.* **2016**, *55*, 9537−9548.
(110) Hu, Z.-B.; Feng, X.; Li, J.; Zhang, Y.-Q.; Yin, L.; Wang, Z.; Ouyang, Z.; Kurmoo, M.; Song, Y. Optimal diamagnetic dilution concentration for suppressing the dipole-dipole interaction in single-ion magnets. *Dalton Trans.* **2020**, *49*, 2159−2167.
(111) Miklovic, J.; Valigura, D.; Boca, R.; Titis, J. A mononuclear Ni(II) complex: a field induced single-molecule magnet showing two slow relaxation processes. *Dalton Trans.* **2015**, *44*, 12484−12487.
(112) Meihaus, K. R.; Rinehart, J. D.; Long, J. R. Dilution-Induced Slow Magnetic Relaxation and Anomalous Hysteresis in Trigonal Prismatic Dysprosium(III) and Uranium(III) Complexes. *Inorg. Chem.* **2011**, *50*, 8484−8489.
(113) Bartolome, J.; Filoti, G.; Kuncser, V.; Schinteie, G.; Mereacre, V.; Anson, C. E.; Powell, A. K.; Prodius, D.; Turta, C. Magneto-structural correlations in the tetranuclear series of $\{Fe_3LnO_2\}$ butterfly core clusters: Magnetic and Moumlssbauer spectroscopic study. *Phys. Rev. B: Condens. Matter Mater. Phys.* **2009**, *80*, No. 014430.

https://dx.doi.org/10.1021/acs.inorgchem.0c01636
Inorg. Chem. 2020, 59, 13281−13294

(114) Vallejo, J.; Castro, I.; Ruiz-Garcia, R.; Cano, J.; Julve, M.; Lloret, F.; De Munno, G.; Wernsdorfer, W.; Pardo, E. Field-Induced Slow Magnetic Relaxation in a Six-Coordinate Mononuclear Cobalt(II) Complex with a Positive Anisotropy. *J. Am. Chem. Soc.* **2012**, *134*, 15704−15707.
(115) Colacio, E.; Ruiz, J.; Ruiz, E.; Cremades, E.; Krzystek, J.; Carretta, S.; Cano, J.; Guidi, T.; Wernsdorfer, W.; Brechin, E. K. Slow Magnetic Relaxation in a Co^{II}-Y^{III} Single-Ion Magnet with Positive Axial Zero-Field Splitting. *Angew. Chem., Int. Ed.* **2013**, *52*, 9130−9134.
(116) Chen, L.; Wang, J.; Wei, J. M.; Wernsdorfer, W.; Chen, X. T.; Zhang, Y. Q.; Song, Y.; Xue, Z. L. Slow Magnetic Relaxation in a Mononuclear Eight-Coordinate Cobalt(II) Complex. *J. Am. Chem. Soc.* **2014**, *136*, 12213−12216.
(117) Suturina, E. A.; Maganas, D.; Bill, E.; Atanasov, M.; Neese, F. Magneto-Structural Correlations in a Series of Pseudotetrahedral $[Co^{II}(XR)_4]^{2-}$ Single Molecule Magnets: An ab Initio Ligand Field Study. *Inorg. Chem.* **2015**, *54*, 9948−9961.
(118) Wernsdorfer, W.; Chakov, N. E.; Christou, G. Determination of the magnetic anisotropy axes of single-molecule magnets. *Phys. Rev. B: Condens. Matter Mater. Phys.* **2004**, *70*, No. 132413.
(119) Krzystek, J.; Zvyagin, S. A.; Ozarowski, A.; Trofimenko, S.; Telser, J. Tunable-frequency high-field electron paramagnetic resonance. *J. Magn. Reson.* **2006**, *178*, 174−183.
(120) Gupta, R.; Taguchi, T.; Lassalle-Kaiser, B.; Bominaar, E. L.; Yano, J.; Hendrich, M. P.; Borovik, A. S. High-spin Mn−oxo complexes and their relevance to the oxygen-evolving complex within photosystem II. *Proc. Natl. Acad. Sci. U. S. A.* **2015**, *112*, 5319−5324.
(121) Lin, Y.-H.; Cramer, H. H.; van Gastel, M.; Tsai, Y.-H.; Chu, C.-Y.; Kuo, T.-S.; Lee, I. R.; Ye, S.; Bill, E.; Lee, W.-Z. Mononuclear Manganese(III) Superoxo Complexes: Synthesis, Characterization, and Reactivity. *Inorg. Chem.* **2019**, *58*, 9756−9765.
(122) Gupta, R.; Taguchi, T.; Borovik, A. S.; Hendrich, M. P. Characterization of Monomeric Mn-II/III/IV-Hydroxo Complexes from X- and Q-Band Dual Mode Electron Paramagnetic Resonance (EPR) Spectroscopy. *Inorg. Chem.* **2013**, *52*, 12568−12575.
(123) Groni, S.; Blain, G.; Guillot, R.; Policar, C.; Anxolabehere-Mallart, E. Reactivity of Mn^{II} with superoxide. Evidence for a $[Mn^{III}OO]^+$ unit by low-temperature spectroscopies. *Inorg. Chem.* **2007**, *46*, 1951−1953.
(124) Neese, F. Calculation of the zero-field splitting tensor on the basis of hybrid density functional and Hartree-Fock theory. *J. Chem. Phys.* **2007**, *127*, 164112.
(125) Maganas, D.; Sottini, S.; Kyritsis, P.; Groenen, E. J. J.; Neese, F. Theoretical Analysis of the Spin Hamiltonian Parameters in $Co^{II}S_4$ Complexes, Using Density Functional Theory and Correlated ab initio Methods. *Inorg. Chem.* **2011**, *50*, 8741−8754.
(126) Neese, F. Importance of Direct Spin−Spin Coupling and Spin-Flip Excitations for the Zero-Field Splittings of Transition Metal Complexes: A Case Study. *J. Am. Chem. Soc.* **2006**, *128*, 10213−10222.
(127) Retegan, M.; Cox, N.; Pantazis, D.; Neese, F. A First-Principles Approach to the Calculation of the on-Site Zero-Field Splitting in Polynuclear Transition Metal Complexes. *Inorg. Chem.* **2014**, *53*, 11785−11793.
(128) Maurice, R.; de Graaf, C.; Guihery, N. Magnetostructural relations from a combined ab initio and ligand field analysis for the nonintuitive zero-field splitting in Mn(III) complexes. *J. Chem. Phys.* **2010**, *133*, No. 084307.
(129) Puzzarini, C.; Barone, V. Toward spectroscopic accuracy for organic free radicals: Molecular structure, vibrational spectrum, and magnetic properties of F_2NO. *J. Chem. Phys.* **2008**, *129*, 084306.
(130) Puzzarini, C.; Barone, V. Toward spectroscopic accuracy for open-shell systems: Molecular structure and hyperfine coupling constants of H_2CN, H_2CP, NH_2, and PH_2 as test cases. *J. Chem. Phys.* **2010**, *133*, 184301.
(131) Perera, S. A.; Watts, J. D.; Bartlett, R. J. A theoretical study of hyperfine coupling constants. *J. Chem. Phys.* **1994**, *100*, 1425−1434.
(132) Perera, S. A.; Salemi, L. M.; Bartlett, R. J. Hyperfine coupling constants of organic radicals. *J. Chem. Phys.* **1997**, *106*, 4061−4066.
(133) Campbell, K. A.; Force, D. A.; Nixon, P. J.; Dole, F.; Diner, B. A.; Britt, R. D. Dual-Mode EPR Detects the Initial Intermediate in Photoassembly of the Photosystem II Mn Cluster: The Influence of Amino Acid Residue 170 of the D1 Polypeptide on Mn Coordination. *J. Am. Chem. Soc.* **2000**, *122*, 3754−3761.

https://dx.doi.org/10.1021/acs.inorgchem.0c01636
Inorg. Chem. 2020, 59, 13281−13294